Modeling Pack Ice as a Cavitating Fluid

GREGORY M. FLATO AND WILLIAM D. HIBLER III

Thayer School of Engineering, Dartmouth College, Hanover, New Hampshire

(Manuscript received 9 July 1990, in final form 22 July 1991)

ABSTRACT

Polar ocean circulation is influenced by fluxes of salt and freshwater at the surface as ice freezes in one location, is transported by the winds and currents, and melts again elsewhere. The motion of sea ice, moreover, is strongly affected by internal stresses that arise from the mechanical strength of the ice cover. A simple sea-ice dynamics model, allowing these effects to be included in large-scale climate studies, is presented. In this model a cavitating fluid behavior is assumed whereby the ice pack does not resist divergence or shear, but does resist convergence. While less realistic than other rheologies that include shear strength, this assumption has certain advantages for long-term climate studies. First, it allows a simple and efficient numerical scheme, in both rectangular and spherical coordinates, which is developed here along with a generalization to include shear strength via the Mohr–Coulomb failure criteria. Second, realistic ice transport is maintained, even when the model is driven by smoothed wind forcing—a feature that may be useful in coupled ice–ocean climate models using mean monthly or mean annual winds. Finally, the lack of shear strength allows smooth flow past an obstacle, making the scheme attractive for coupling to a global ocean circulation model using an artificial island to avoid the mathematical singularity at the North Pole. Noteworthy, however, is the fact that the numerical scheme developed here does not require an island at the pole, making the model equally suited for coupling to a global atmospheric circulation model.

Three-year dynamic–thermodynamic simulations using observed forcing from 1981 to 1983 are performed using the cavitating fluid model and a more complete viscous-plastic model for comparison. The thickness buildup patterns, net ice growth, atmospheric heat flux, and total ice volume calculated by the cavitating fluid model are very similar to the viscous-plastic model results; however, the cavitating fluid model substantially overestimates local ice drift when compared to observed buoy drift. A 3-year simulation using the spherical grid version of the model, both with and without an artificial island at the pole, shows that the island has little impact on the thickness buildup and ice transport. Overall, the cavitating fluid approximation is shown to be a useful simplification, allowing essential feedbacks between ocean circulation and ice transport to be efficiently included in large-scale climate studies.

1. Introduction

The influence of the polar oceans on global climate is substantially determined by the movement, extent, and makeup of their ice covers. An ice cover provides an effective insulating blanket, impeding the exchange of heat between the atmosphere and ocean, and a relatively reflective surface, reducing the incoming shortwave radiation. The insulating effectiveness of an ice cover is strongly dependent on its thickness, or more precisely, since pack ice is composed of a variety of thicknesses, on the areal fraction of each thickness. Of particular importance is the fraction of open water (ice of zero thickness) through which a large portion of the heat exchange takes place. Ice transport can also have an important effect, particularly on ocean circulation, in that it allows ice to form in one location and melt in another, thus creating a net imbalance of salt flux at the ocean surface.

A sea-ice cover is not a static, uniformly thick layer, but rather is a constantly changing amalgam of open water, thin first year ice, thick multiyear ice, and even thicker ridged ice. Virtually any motion of the pack will result in a redistribution of the amount of ice in each of these categories; in particular, a deformation event will transform thin ice into thick ice by ridging and simultaneously create areas of open water. The exchange of heat between the ocean, ice, and atmosphere may cause a decrease in thickness of all categories of ice, through melting, or an increase in thickness, through freezing, with the increase of thickness most pronounced for very thin ice or open water. Considerable effort has been made to properly include these thermodynamic processes in climate models (e.g., Maykut and Untersteiner 1971; Semtner 1976; Parkinson and Washington 1979). However, because thickness buildup and open water formation are so dominated by dynamic processes, the inclusion of some sea-ice dynamics parameterization in climate models is also necessary to allow for the potentially important feedback between thermodynamic processes, ice transport, and deformation.

Corresponding author address: Dr. Gregory M. Flato, Thayer School of Engineering, Dartmouth College, Hanover, NH 03755.

A second feature of the large-scale behavior of sea ice is the observation that it is strongly resistant to convergence and yet relatively free to diverge. This can be understood by noting the similarity of pack ice to a granular medium—a collection of discrete particles (ice floes) separated by cracks and leads. Although this granular analog more accurately describes the ice pack at small scales, at large scales it is more convenient to invoke the continuum hypothesis and describe the aggregate behavior in terms of rheology (the mathematical description of deformation and flow under load). It is this rheology that relates the change in structure of an ice cover to the forces applied by winds and currents and is therefore the key to modeling ice dynamics. Plastic rheologies have been used successfully in the past (e.g., Coon et al. 1974; Hibler 1979, 1980) and the sensitivity of ice drift to a number of different rheologies has been investigated by Ip et al. (1991).

The motivation for the present work is the development of a sea-ice dynamics parameterization, which retains most of the essential physics of large-scale drift, is conceptually and computationally simple, and is well suited to large-scale, crude resolution climate studies. We note that the approach can be viewed as a reformulation of the velocity correction method of Nikiforov et al. (1967) and Parkinson and Washington (1979) to approximate the so-called cavitating fluid rheology. In this scheme, the ice pack is assumed to have no shear strength which, although counterintuitive, has certain advantages: The model is very simple to formulate and implement, and a more robust (and realistic) circulation of the ice is maintained for wind fields averaged over periods of days or weeks (Flato and Hibler 1990). In addition, the large-scale thickness buildup and heat transfer patterns calculated by this model are very similar to the more complete viscous-plastic model of Hibler (1979, 1980). As discussed in more detail later, the velocity correction scheme developed here has the advantage over previous ad hoc methods in that an attempt is made to conserve momentum and the resulting velocity field is consistent with an internal ice pressure field, calculated simultaneously.

The aim of this paper is to present the numerical formulation of the cavitating fluid rheology, both in rectangular and spherical coordinates, and to demonstrate its utility by incorporating the cavitating fluid rheology into a complete dynamic–thermodynamic sea-ice model and performing several 3-year simulations of the Arctic ice cover. Comparison with observed buoy drift and the more complete viscous-plastic model of Hibler (1979) yields insight into the effects of this simplified parameterization. In addition, an extension of the numerical scheme to include shear strength via a nonlinear shear viscosity (the Mohr–Coulomb rheology) is briefly discussed.

2. Model description

a. Governing equations

Following Hibler (1979), the momentum balance for sea ice is described by the following vector equation

$$m\frac{\partial \mathbf{u}}{\partial t} = -mf\mathbf{k}\times\mathbf{u} + \tau_a + \tau_w - mg\nabla H + \mathbf{F} \quad (1)$$

where the nonlinear momentum advection term has been neglected, m is the mass of ice per unit area, $\mathbf{u}$ is the ice velocity, t is time, f is the Coriolis frequency, $\mathbf{k}$ is the upward unit normal, τ_a and τ_w are forces (per unit area) due to air and water drag, respectively, g is the acceleration due to gravity, H is the sea-surface dynamic height, and $\mathbf{F}$ is the force (per unit area) due to variations in internal ice stress. Note that here and in the remainder of the paper, boldface characters represent vector quantities. The air- and water-drag stresses are obtained from a simple quadratic formulation (e.g., McPhee 1975)

$$\tau_a = C_a^*[\mathbf{U}_a\cos\phi + \mathbf{k}\times\mathbf{U}_a\sin\phi] \quad (2)$$

$$\tau_w = C_w^*[(\mathbf{U}_w - \mathbf{u})\cos\theta + \mathbf{k}\times(\mathbf{U}_w - \mathbf{u})\sin\theta] \quad (3)$$

where

$$C_a^* = \rho_a C_a|\mathbf{U}_a|$$

$$C_w^* = \rho_w C_w|\mathbf{U}_w - \mathbf{u}|$$

and $\mathbf{U}_a$ and $\mathbf{U}_w$ are the geostrophic wind and current velocities, C_a and C_w are wind and water-drag coefficients (taken to be 0.0012 and 0.0055, respectively); ϕ and θ are wind and water turning angles (both of which are taken to be 25°).

The internal ice-stress term depends on the particular parameterization chosen to represent the relationship between ice velocity (deformation) and the applied forces. It is a particular approach to this parameterization, the cavitating fluid rheology, and its numerical formulation that is the main theme of the present paper.

The cavitating fluid rheology attempts to capture the most important aspects of sea-ice behavior while remaining computationally simple. This is achieved by making some simplifying assumptions regarding the large-scale behavior of pack ice. The fundamental assumption is that pack ice can be thought of as an idealized two-phase medium in which one phase (open water) has no strength at all, while the other phase (ice) is relatively rigid. This idealized medium has no shear or tensile strength and so divergence is allowed to occur freely causing only an increase in the area covered by the open water phase (i.e., a reduction in compactness). In compression, the medium has some resistance due to the "rigid" phase. It should be noted that the ice phase need not be completely rigid, but may have a compressive strength beyond which convergence and

thickening may occur. This compressive strength can be considered a function of both the ice thickness and compactness. As will be shown later, this idealized behavior is conveniently modeled numerically.

To put this rheology into the context of others that have been used, it is useful to consider a plot of the failure surface in principal stress space.[1] The cavitating fluid failure surface in two dimensions plots simply as a line in the third quadrant starting at the origin and inclined 45° from the horizontal axis as shown in Fig. 1. The length of the line depends on the compressive strength of the material with completely incompressible behavior represented by a line extending to infinity. This may be made more clear by comparison with the elliptical yield curve used by Hibler (1979), which is shown also in Fig. 1. Inside the ellipse, the material is supposed to be rigid (although for numerical purposes a very small amount of viscous creep is allowed in practice) while on the curve, plastic flow occurs subject to the so-called "normal-flow rule." This means that the strain-rate vector is normal to the yield curve in a coordinate system with principal stresses and principal strain rates aligned. If one now imagines deforming the ellipse such that the ratio of major to minor axes gets larger and larger, one will obtain the cavitating fluid behavior in the limit as the ratio goes to infinity. Keeping the normal-flow rule in mind, this thought experiment also shows that convergence and divergence can occur only at the two endpoints of the cavitating fluid line (compressive and tensile failure) while all other points on the line represent incompressible, pure shear behavior. The internal ice-stress term in Eq. (1) can now be expressed simply as

$$\mathbf{F} = -\nabla p \tag{4}$$

where p is the internal ice pressure (equal to the magnitude of the two principal stresses).

Perhaps the most important ramification of assuming the aforementioned cavitating fluid behavior is that shear strength is neglected. For the present, this simplification can be thought of as heuristic and will be shown to produce a reasonable sea-ice model for long-term climate studies. The ramifications of this assumption will be examined by comparison with a more complete model and by comparison with large-scale observations of buoy drift.

The essential features of the numerical scheme to implement the cavitating fluid rheology are not new; Nikiforov et al. (1967) used a similar scheme in their model of nearshore ice flow in the east Siberian and Chukchi seas. The basic idea is to start with free drift,

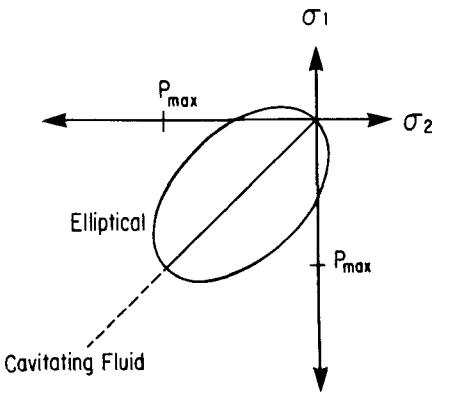

FIG. 1. Elliptical and cavitating fluid yield curves in principal stress space.

that is, the ice velocity field calculated by ignoring ice interaction, and then correct these velocities in a manner that reflects the compressive strength of the pack ice. In the model of Nikiforov et al. (1967), this correction was simply to remove the onshore component of velocity when the compactness reached 100%. A similar scheme was used by Parkinson and Washington (1979) in a large-scale dynamic–thermodynamic sea-ice model. In their scheme, the inward velocity components at any computational grid cell were reduced in an iterative fashion so that the compactness remained at or below a specified amount. Flato and Hibler (1990) showed that these schemes excessively damp the velocity field by not conserving momentum and presented a conservative method that approximately solved the equations of motion. The numerical scheme presented in section 2b preserves the spirit of these ad hoc schemes in that it is a correction to free drift; however, the correction conserves momentum and yields a complete solution to the equations of motion, which is consistent with an internal ice pressure field. An important aspect of the present numerical scheme is that the internal ice pressure is explicitly calculated. Aside from providing a rationale for the velocity correction, the pressure calculation can be used, in conjunction with an assigned failure strength, to allow convergence and so provide a mechanism for dynamic increase of ice thickness.

b. Numerical scheme

Recalling the idealized cavitating fluid rheology discussed in section 2a, the ice pack is assumed to have no shear or tensile strength, but does resist compression via internal ice pressure. What we wish to calculate is the velocity and pressure fields satisfying the equation of motion (1) and the conditions that 1) p be zero if there is a divergent component to the velocity field and 2) equal to the compressive strength if there is a con-

[1] The failure surface defines the stress states at which plastic flow occurs; points within the surface represent rigid behavior, points on the surface represent plastic flow, and points outside cannot be reached.

vergent component. The theme here is to begin with velocity and pressure fields, which satisfy the equation of motion (1), and modify these fields in such a way as to satisfy the above constraints. Of course the simplest initial velocity field is the so-called free-drift velocity, that is, the velocity field satisfying Eq. (1) with $p = 0$ everywhere; however, the fact that any solution to Eq. (1) can be used as the initial field will be useful later on. We note that another approach to solving these equations is to use a nonlinear bulk viscosity and directly integrate the equations of motion. As discussed below, this procedure will yield the same result but is computationally much less efficient.

We begin by noting that, neglecting the acceleration term, the equation of motion (1) can be written in the following compact form,

$$-\alpha\mathbf{u} + \beta\mathbf{k} \times \mathbf{u} + \tau = \nabla p \tag{5}$$

where $\alpha = C_w^* \cos\theta$ and $\beta = mf + C_w^* \sin\theta$; τ is the force vector of those terms in the momentum balance that do not depend on $\mathbf{u}$ (namely, air drag, sea-surface tilt, and water drag due to geostrophic ocean currents). We now seek the corrected fields $\mathbf{u} + \tilde{\mathbf{u}}$ and $p + \tilde{p}$ (where $\tilde{}$ indicates a correction) such that $p + \tilde{p} \geq 0$ and

$$\begin{aligned} \nabla\cdot(\mathbf{u} + \tilde{\mathbf{u}}) &\geq 0 \quad \text{if} \quad p + \tilde{p} = 0 \\ \nabla\cdot(\mathbf{u} + \tilde{\mathbf{u}}) &= 0 \quad \text{if} \quad 0 < p + \tilde{p} < p_{\max} \\ \nabla\cdot(\mathbf{u} + \tilde{\mathbf{u}}) &\leq 0 \quad \text{if} \quad p + \tilde{p} = p_{\max} \end{aligned} \tag{6}$$

where $p_{\max}$ is the maximum allowable pressure or ice strength, and furthermore, these corrected fields satisfy the equation of motion, namely,

$$-\alpha(\mathbf{u} + \tilde{\mathbf{u}}) + \beta\mathbf{k} \times (\mathbf{u} + \tilde{\mathbf{u}}) + \tau = \nabla(p + \tilde{p}). \tag{7}$$

If we now subtract Eq. (5) from Eq. (7) and write the result in component form, we can solve for the velocity corrections in terms of the pressure correction $\tilde{p}$ and then obtain an equation for the $\tilde{p}$ so that the conditions on the divergence rate (6) can be satisfied. However, for reasons that will be discussed shortly, such a scheme is difficult to implement numerically. On the other hand, if we approximate (7) by

$$-\alpha(\mathbf{u} + \tilde{\mathbf{u}}) + \beta\mathbf{k} \times \mathbf{u} + \tau = \nabla(p + \tilde{p}) \tag{8}$$

that is, assume the off-diagonal terms are constants determined by the initial velocity field, the situation is greatly simplified. (In fact, the off-diagonal terms will be better approximated by imbedding the correction scheme within the time-marching procedure as discussed later.) Now (5) can be subtracted from (8) to give the following equation for the velocity correction,

$$\tilde{\mathbf{u}} = \frac{-1}{\alpha} \nabla\tilde{p}. \tag{9}$$

We now require an expression for $\tilde{p}$ such that $\nabla\cdot(\mathbf{u} + \tilde{\mathbf{u}}) = 0$. Thus, we obtain from (9),

$$\nabla\cdot\left(\frac{1}{\alpha}\nabla\tilde{p}\right) = \nabla\cdot\mathbf{u} \tag{10}$$

where we note that if α is constant, we have an equation for the Laplacian of $\tilde{p}$ in terms of the divergence rate of the velocity field before correction. At this point it appears that we have a very complicated situation in which we require a solution to (9) and (10) subject to the cavitating fluid conditions (6); however, in finite-difference form the situation simplifies considerably and an iterative, relaxation solution can be obtained.

Before proceeding with the finite-difference formulation, some consideration must be given to the computational grid. Two grid schemes commonly used in problems of this kind are the Arakawa B and C grids. The B grid was initially used (Flato and Hibler 1989, 1990) to be consistent with the ice dynamics model of Hibler (1979) and many of the large-scale ocean circulation models. It was found that, due to the Laplacian form of Eq. (10), the B-grid formulation suffers from an alternating grid point or "checkerboard" instability, which is not present in the C-grid formulation. This is discussed in more detail in appendix A. For this reason the Arakawa C staggered grid formulation, depicted in Fig. 2, will be used. An unfortunate side effect of this choice is that calculation of the free-drift velocity field requires an iterative relaxation solution (as opposed to the simple algebraic solution possible in the B grid); however, the free-drift solution scheme converges very quickly and so does not add significantly to the overall computational effort. It should be noted here that the alternating gridpoint instability only becomes obvious when completely incompressible behavior is modeled. Therefore, in most cases the velocity and thickness fields calculated by the B-grid model are very similar to those of the C-grid version. A comparison of the thickness fields calculated by both versions of the model is made in appendix A.

The derivation that follows will use a rectangular grid in a Cartesian coordinate system; the analogous

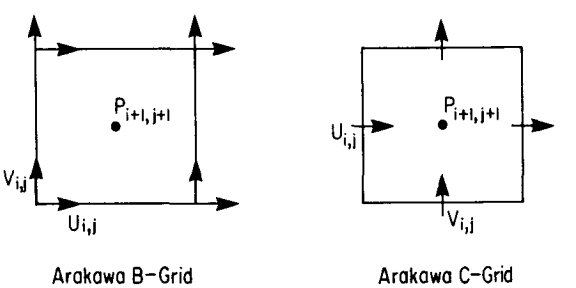

FIG. 2. Computational grid cells showing location of vector and scalar quantities. (a) Arakawa B grid, (b) Arakawa C grid.

equations for a spherical grid are presented in appendix B. In the C grid, the finite-difference form for the left-hand side of Eq. (10) is

$$\nabla\cdot\left(\frac{1}{\alpha}\nabla\tilde{p}\right) = \frac{1}{\Delta x^2}\left[\frac{1}{\alpha^x_{i+1,j}}(\tilde{p}_{i+2,j+1}-\tilde{p}_{i+1,j+1}) - \frac{1}{\alpha^x_{i,j}}(\tilde{p}_{i+1,j+1}-\tilde{p}_{i,j+1})\right] + \frac{1}{\Delta y^2}\left[\frac{1}{\alpha^y_{i,j+1}}(\tilde{p}_{i+1,j+2}-\tilde{p}_{i+1,j+1}) - \frac{1}{\alpha^x_{i,j}}(\tilde{p}_{i+1,j+1}-\tilde{p}_{i+1,j})\right] \quad (11)$$

where α^x_{ij} is the coefficient for the x-velocity component and α^y_{ij} is the coefficient for the y-velocity component. The simplification now comes because we will be performing a relaxation solution on the pressure field and so at any point in the relaxation sweep, we will be incrementing p only at the $i+1, j+1$ location. Therefore, only $\tilde{p}_{i+1,j+1}$ is nonzero and so, combining (10) and (11), we get

$$\tilde{p}_{i+1,j+1} = -\nabla\cdot\mathbf{u}\Big/\left\{\frac{1}{\Delta x^2}\left[\frac{1}{\alpha^x_{i,j}}+\frac{1}{\alpha^x_{i+1,j}}\right] + \frac{1}{\Delta y^2}\left[\frac{1}{\alpha^y_{i,j}}+\frac{1}{\alpha^y_{i,j+1}}\right]\right\}. \quad (12)$$

The concomitant velocity corrections for this grid cell are given by the finite-difference form of (9) as

$$\tilde{u}_{i,j} = \frac{-1}{\alpha^x_{i,j}}\frac{\tilde{p}_{i+1,j+1}}{\Delta x}$$

$$\tilde{u}_{i+1,j} = \frac{1}{\alpha_{i+1,j}}\frac{\tilde{p}_{i+1,j+1}}{\Delta x}$$

$$\tilde{v}_{i,j} = \frac{-1}{\alpha^y_{i,j}}\frac{\tilde{p}_{i+1,j+1}}{\Delta y}$$

$$\tilde{v}_{i,j+1} = \frac{1}{\alpha^y_{i,j+1}}\frac{\tilde{p}_{i+1,j+1}}{\Delta y}. \quad (13)$$

Equations (12) and (13) give the corrections to be added to the pressure and velocities at a grid cell such that the divergence in the grid cell, calculated by

$$\nabla\cdot\mathbf{u} = \frac{1}{\Delta x}(u_{i+1,j}-u_{i,j}) + \frac{1}{\Delta y}(v_{i,j+1}-v_{i,j}) \quad (14)$$

will be exactly zero.

Having now derived all the necessary equations, the relaxation procedure for calculating cavitating fluid pressure and velocity fields can now be outlined. The basic idea is to begin with velocity and pressure fields that satisfy Eq. (5) and then sweep through the computational grid a number of times applying the appropriate corrections grid cell by grid cell. The current value of either velocity or pressure is the sum of the initial value and all of the corrections that have been applied. At a given grid cell, the first step is to calculate the present divergence rate from Eq. (14) (note that if the divergence rate is calculated using the most recent values for u and v, we have the Guass–Seidel relaxation scheme).[2] If the divergence rate is greater than zero (i.e., diverging) and the pressure is also zero, then nothing need be done (i.e., $\tilde{u}=0$, $\tilde{v}=0$, and $\tilde{p}=0$). If, on the other hand, the divergence is negative (i.e., converging), the corrections of Eqs. (12) and (13) are calculated and the velocity and pressure fields updated. In addition, the following special cases need to be considered: 1) if the divergence is positive and the pressure is finite either the correction based on (12) or $\tilde{p}=-p$ is applied, whichever is smaller in magnitude (this ensures that after correction either the pressure is finite and the divergence is zero or the pressure is zero and the divergence positive); 2) if the new pressure, $p+\tilde{p}$ is greater than $p_{\max}$, the pressure correction $\tilde{p}=p_{\max}-p$ and the concomitant velocity corrections must be used (this ensures that the pressure never gets above the specified ice strength).

Since the correction applied to one grid cell influences the divergence rate of all its neighbors, the corrections must be applied in an iterative manner, sweeping through the computational grid a number of times until the change in velocity between one sweep and the next is smaller than some specified tolerance. It is useful to note that the above corrections applied to a particular grid cell can only cause convergence in neighboring grid cells and so, if the initial field is free drift, case (1) will never be encountered. Also, if completely incompressible flow is to be modeled (i.e., $p_{\max}\to\infty$), case (2) will never be encountered.

It is instructive here to consider briefly the special case of $\Delta x=\Delta y$ and $\alpha_{i,j}$ equal to a constant. In this case, we note first that the sum of velocity magnitudes over a grid cell is the same before and after correction (except near boundaries), and so, in the limit of uniform thickness, the average momentum is conserved by the correction. Moreover, Flato and Hibler (1990) pointed out that in this case the correction also results in a decrease in the sum of the velocities squared ensuring convergence of the relaxation scheme. In the more general case described above, these simple precepts no longer apply; nevertheless, the relaxation scheme has always converged based on numerous tests.

The reason for approximating (7) by (8) is clear if one considers that, in the C grid, the velocity in the off-diagonal term of (7) would have to be calculated from a four-point average, thereby eliminating the

[2] Note that a Jacobi scheme in which (12) is computed using the velocities from the previous step in the iteration, can also be used and lends itself to implementation on massively parallel computers.

possibility of simple pressure–velocity relationships like Eq. (13). (Note that in the B grid, the appropriate pressure–velocity relationships are easy to find, however, the B grid is undesirable for the reasons discussed earlier.) In addition, the pressure field calculated by this approximate procedure is quite close to the final pressure field, and so, an accurate solution can be obtained by performing the correction procedure twice for each time step, as discussed next.

It should be noted at this point that the solution obtained by the present scheme has been verified by comparison to a direct, forward Euler time-stepping solution (Ip et al. 1991) similar to that used by Semtner (1987). This is a much less efficient procedure, but does give a solution with known accuracy. The cavitating fluid correction scheme produces equilibrium velocity fields that are within 1% of those produced by the direct time-stepping scheme (Ip et al. 1991).

In order for the aforementioned cavitating fluid algorithm to be incorporated into a complete dynamic sea-ice model it must be stepped forward in time. The nonlinear water-drag terms in Eq. (3) (which appear in the coefficients α and β in the preceeding section) require a two-step time-stepping scheme like the modified Euler method. Since this requires calculating the velocity and pressure fields twice for each time step, a predictor–corrector scheme can be used for the off-diagonal terms in the cavitating fluid procedure. In other words, we can start with free drift and obtain the corrected fields for the first step, calculate new drag coefficients based on this new velocity field, and then calculate a "modified" free-drift field [from (5)] using these new drag coefficients and the pressure field from the first step. This modified free-drift field then becomes the initial field to which the cavitating fluid correction scheme is applied to obtain the final velocity and pressure fields. (This is one reason for deriving the cavitating fluid corrections with an arbitrary initial pressure field.) This scheme is represented symbolically as follows:

$$-\alpha(u^\kappa)\mathbf{u}^{\kappa+1/2} + \beta(u^\kappa)\mathbf{k} \times \mathbf{u}^f + \tau = \nabla p^{\kappa+1/2} \quad (15a)$$

$$-\alpha\left(\frac{u^\kappa + u^{\kappa+1/2}}{2}\right)\mathbf{u}^{\kappa+1} + \beta\left(\frac{u^\kappa + u^{\kappa+1/2}}{2}\right)\mathbf{k} \times \mathbf{u}^{\kappa+1/2} + \tau = \nabla p^{\kappa+1} \quad (15b)$$

where $\mathbf{u}^f$ is the free-drift velocity field; superscript κ indicates the time step, and the arguments of α and β indicate the velocity magnitudes used to calculate the nonlinear drag coefficient (3). This scheme works well because the pressure field calculated in (15a) is very close to the pressure field one obtains if the above scheme is stepped forward many times without changing the forcing τ. It might also be noted here that the free-drift velocity, $\mathbf{u}^f$, could be replaced by $\mathbf{u}^\kappa$ (and the initial pressure field of zero replaced by p^κ), which might result in improved efficiency if the forcing is slowly varying.

c. *Extension of cavitating fluid scheme to include shear strength*

Although the cavitating fluid scheme was developed as a simple sea-ice dynamics parameterization in which the lack of shear strength is a fundamental assumption, the scheme can be generalized to include shear strength via a nonlinear shear viscosity in a manner similar to that of the viscous-plastic model of Hibler (1979). In particular, the Mohr–Coulomb failure criterion, commonly used in soil mechanics, can be simulated with results almost identical to the direct integration method (Ip et al. 1991) but with much less computational effort.

The Mohr–Coulomb failure criterion is a linear relationship between pressure and shear strength and plots as two lines in principal stress space, as shown in Fig. 3. In other words, increasing pressure produces increasing shear strength. The angle between the two failure lines is related to the more common "angle of shearing resistance," φ, by the following definition:

$$\sin\varphi = \tan\frac{\delta}{2}. \quad (16)$$

Unlike most soil-mechanics problems, the sea-ice case is essentially a two-dimensional problem in which the pressure cannot increase without bound; therefore, a limiting pressure or "cap" must be placed on the yield curve as shown in Fig. 3. As in the case of the elliptical yield curve, stress states on the failure surface represent plastic flow while stress states inside represent rigid behavior. In contrast to the elliptical yield curve however, the normal-flow rule will not be applied to the Mohr–Coulomb case since this would imply dilation for most of the yielding stress states; rather, stress states on the two limbs of the Mohr–Coulomb yield curve correspond to pure shear deformation.

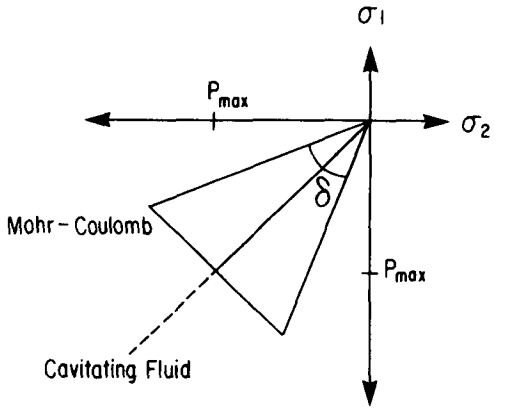

FIG. 3. Mohr–Coulomb failure envelope showing included angle, δ, and cavitating fluid yield curve for comparison.

Recalling that the cavitating fluid scheme calculates a velocity and pressure field based on no shear resistance, one can imagine starting with such a solution, calculating a shear strength at each location based on the Mohr–Coulomb criterion, and applying an additional correction procedure to reduce the shear deformation. This can be accomplished by introducing a nonlinear shear viscosity at each point and performing a relaxation solution based on these shear viscosities and the pressure field from the cavitating fluid correction. The numerical details of the Mohr–Coulomb model are given in appendix C, and some preliminary results are given in section 3. It is not, however, the purpose of this paper to investigate the effect of this particular shear strength parameterization, but rather to present the numerical method as an extension of the cavitating fluid model.

d. Strength parameterization

The large-scale compressive strength of sea ice, $p_{\max}$, can be parameterized in a number of ways depending on the process being modeled. The simplest such parameterization is to ignore ice interaction altogether and set $p_{\max} = 0$ (i.e., free drift). The simplest parameterization that allows for ice interaction is to consider the pack to be completely incompressible, that is, $p_{\max} \to \infty$. This is also not a particularly useful parameterization for long-term integrations because it neglects the important process of dynamic thickness buildup and, in addition, requires substantially more computational effort than the case of a reasonable ice strength. Perhaps the next simplest parameterization is to consider the ice pack to be incompressible if its thickness exceeds some specified cutoff value while remaining free to converge for smaller thicknesses. Such a scheme, when integrated for a several month period, produces an ice cover that is nearly all at the cutoff thickness and requires as much or more computational effort than the more realistic parameterization discussed next.

A more physical parameterization is that suggested by Hibler (1979), which is

$$p_{\max} = p^* h \exp[-K(1 - A)] \qquad (17)$$

where p^* and K are empirical constants taken to be 27.5 kN m^{-2} and 20, respectively; h is the ice thickness (m), and A is the compactness (or ice-covered area fraction, a number between 0 and 1). The value for p^* was determined by Hibler and Walsh (1982) based on comparisons with the observed drift of a Soviet ice station, while K was chosen (Hibler 1979) to reproduce the observation that pack ice with more than about 10% open water exhibits very little resistance to convergence.

e. Thermodynamic growth and advection

The solution of the momentum equation was discussed in some detail above, but we have yet to discuss the continuity equations that, in the case of the two-level model considered here, can be written as

$$\frac{\partial h}{\partial t} = -\nabla \cdot (\mathbf{u}h) + G_h \qquad (18a)$$

$$\frac{\partial A}{\partial t} = -\nabla \cdot (\mathbf{u}A) + G_A \qquad (18b)$$

where G_h and G_A are the thermodynamic growth rates of ice and compactness, respectively. The thermodynamic growth terms are modeled essentially the same as Parkinson and Washington (1979), except that snow cover is not explicitly included and there is a constant oceanic heat flux, which is taken from the diagnostic ice–ocean calculation of Hibler and Bryan (1987). The thermodynamic calculations are discussed in more detail in Hibler (1980, appendix B) and Hibler and Walsh (1982). The advection terms are calculated using simple upstream differencing.

3. Simulation results

a. Computational grid and forcing fields

The numerical results described in this section were obtained by applying the cavitating fluid model to a 160-km resolution Cartesian grid representing the Arctic Ocean, Barents Sea, and parts of the Norwegian and Greenland seas, as shown in Fig. 4. The time step

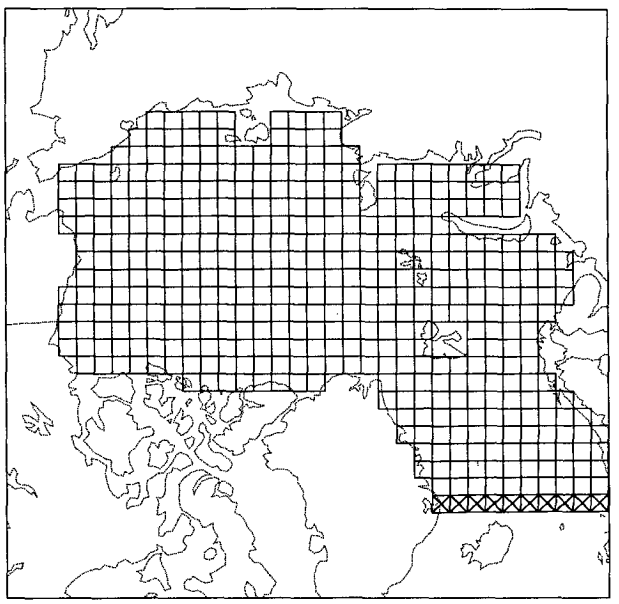

FIG. 4. Computational grid used in simulations. Grid cells are 160 km square with cross-hatched cells indicating outflow boundaries.

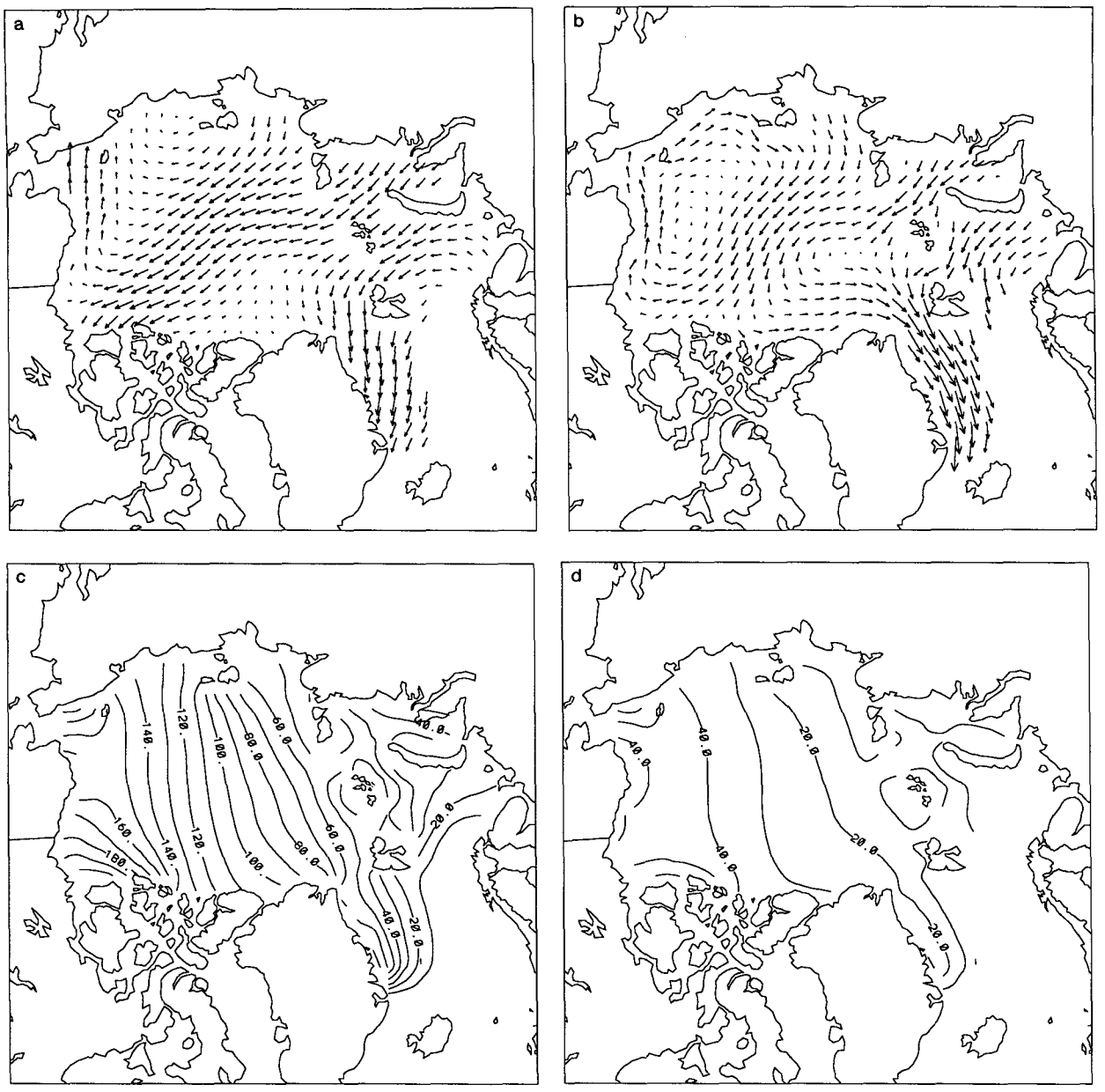

FIG. 5. Monthly average velocity fields for March 1983; a vector one grid cell long is approximately 0.1 m s^{-1}; (a) free drift; (b) incompressible cavitating fluid. Monthly average pressure fields for March 1983; contour interval is 10 kN m^{-1}; (c) incompressible cavitating fluid; (d) cavitating fluid with compressive strength.

is 1 day. Lateral boundary conditions are "no slip" at land boundaries (for the viscous-plastic model) and free outflow to the North Atlantic, as described by Hibler (1979) through the cross-hatched grid cells in the figure. The model results presented make use of forcing fields for the period January 1981–December 1983; however, to ensure a reasonable initial state, the model was allowed a 3-yr "spinup" period with a climatological dataset.

The forcing fields for the climatological spinup period were obtained from the following sources. The wind fields are based on the NMC analysis of the "FGGE" year, December 1978–November 1979, with the mean replaced by twice the 30-yr mean of the 1951–80 wind fields described by Walsh et al. (1985). This gives a wind field with realistic daily variability yet produces mean circulation and thickness buildup representative of climatology. (The idea here was simply to

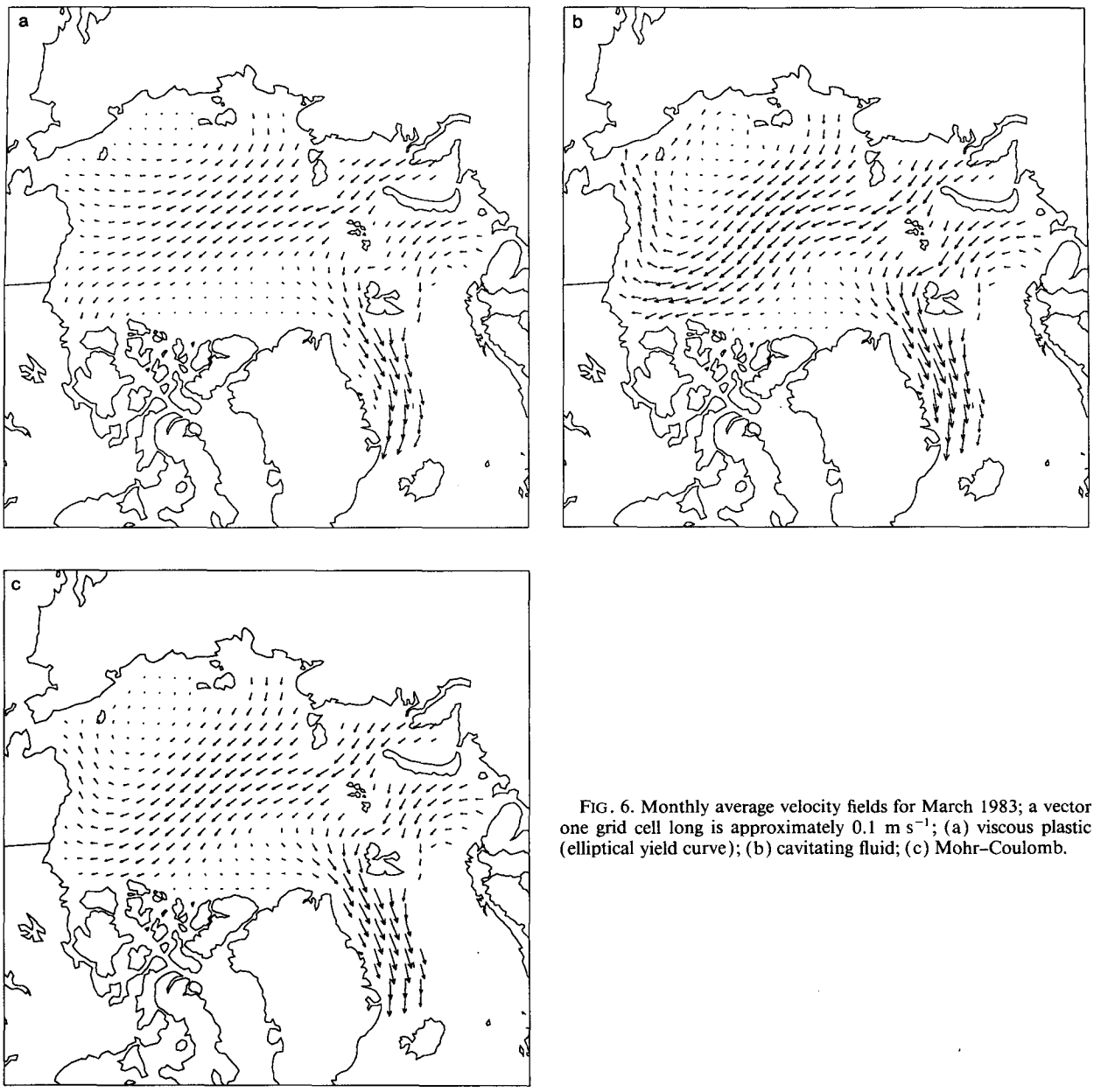

FIG. 6. Monthly average velocity fields for March 1983; a vector one grid cell long is approximately 0.1 m s^{-1}; (a) viscous plastic (elliptical yield curve); (b) cavitating fluid; (c) Mohr–Coulomb.

construct a wind field that produced a thickness field similar to the long-term mean so as to provide a reasonable initial condition for the simulations using the observed wind fields from 1981 to 1983). The air temperature and humidity data were taken from Crutcher and Meserve (1970), and the radiation data was calculated as in Parkinson and Washington (1979). The average annual oceanic heat flux and the geostrophic ocean currents (approximated by the average annual surface currents) are from the diagnostic ice–ocean calculation of Hibler and Bryan (1987). The 1981–83 dataset also uses this average annual heat flux, but the wind fields were calculated from the NCAR surface-pressure analysis and the thermodynamic fields from the NASA analysis (J. Walsh, personal communication).

b. Velocity patterns and long-term drift

The results discussed in this section are meant to illustrate the effect of neglecting shear resistance in the cavitating fluid velocity model on the velocity patterns and ice transport. The thickness buildup and the feedback between dynamics and thermodynamics will be

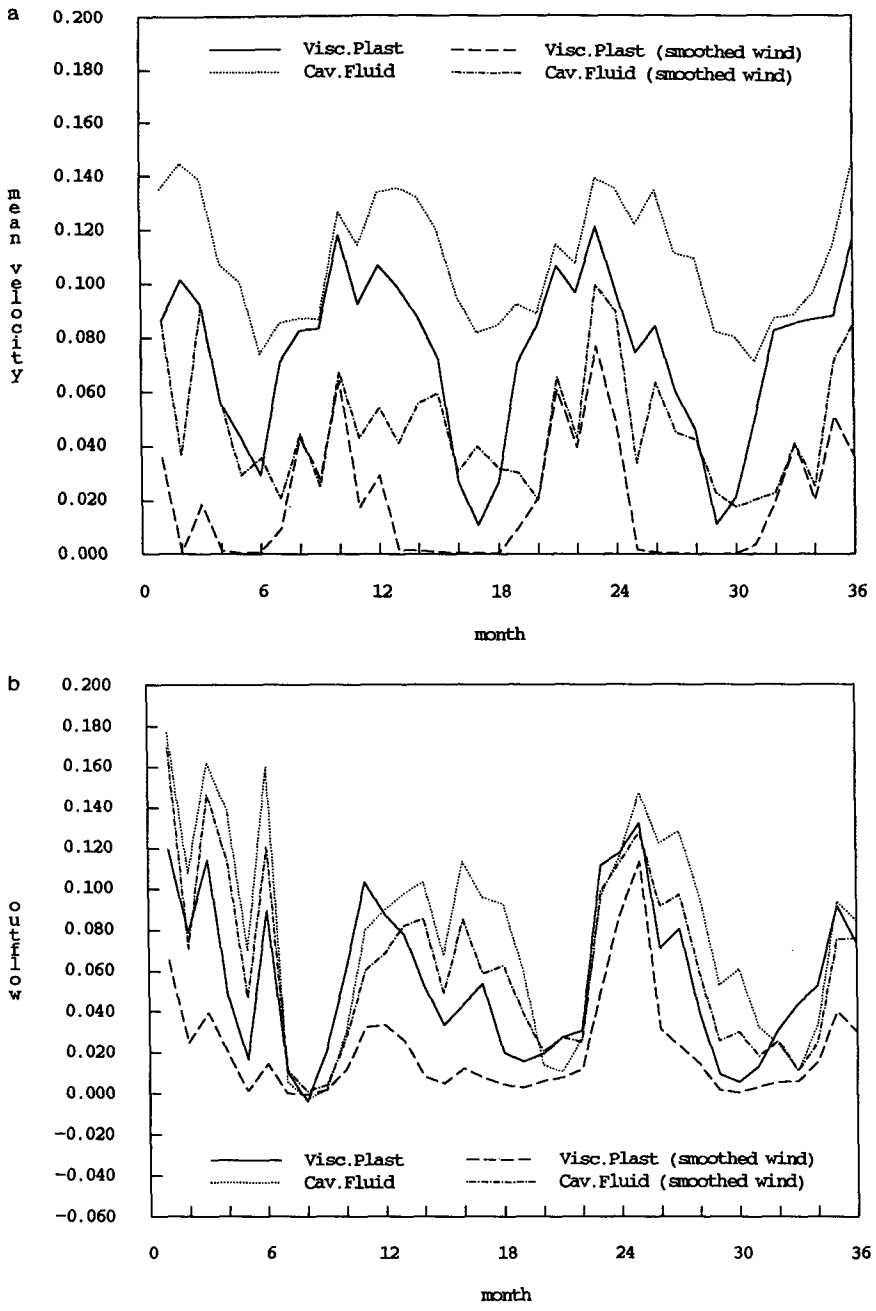

FIG. 7. Time series of (a) monthly average velocity magnitude (m s^{-1}) in the Arctic basin and (b) monthly average ice outflow (Sv $\equiv 10^6$ m^3 s^{-1}) through the Fram Strait, for the period 1 January 1981 to 31 December 1983. Results for both daily varying and monthly averaged wind forcing are shown.

examined in the following sections. Figure 5 illustrates the main points here, showing monthly average velocity and pressure fields for March 1983. The average free-drift velocity field is shown in Fig. 5a. Of particular note is the strong flow converging against the Canadian Archipelago. The velocity field calculated by the incompressible cavitating fluid model in Fig. 5b illustrates how the correction scheme removes this convergence by "steering" the flow alongshore creating a double gyre. It is interesting to also note the similarity between this behavior and that of the Stommel (1948) ocean model (wherein the curl produced by a latitudinally

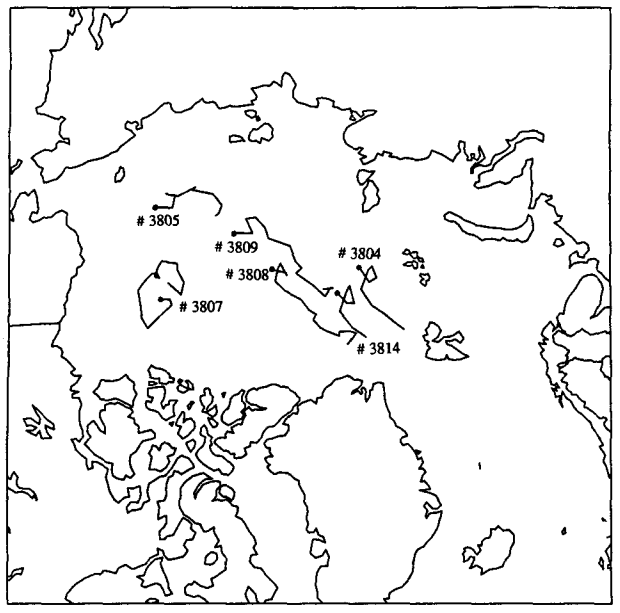

FIG. 8. Observed buoy tracks showing positions at the middle of each month starting 15 June 1981.

varying wind field is manifested as an ocean gyre). In fact, for a closed basin, the analogy between the incompressible cavitating fluid model and the Stommel ocean model is exact, and the numerical scheme has been tested in this context.

As the cavitating fluid model affects change on the free-drift velocity field by adding internal ice pressure, it is no surprise that the highest average pressures, shown in Fig. 5c, are in the Beaufort Sea region where the most drastic alterations were required. Also of interest is the magnitude of the monthly average pressures required to resist all convergence—nearly 200 kN m^{-1} in places. Of course, daily values of ice pressure can be larger still. When the ice is allowed a compressive strength [Eq. (17)], these high pressures are not reached, as shown in Fig. 5d, and so some convergence remains.

The effect of neglecting shear strength in the cavitating fluid is demonstrated by comparison with the widely used Hibler (1979) viscous-plastic model, which employs an elliptical yield curve with shear strength equal to half of the compressive strength, as well as the Mohr–Coulomb model discussed briefly in the previous section and in appendix C. The compressive strength parameterization [Eq. (17)] is used in all three models. The average velocity fields for March 1983 (Figs. 6a,b, and c) show that the lack of shear resistance in the cavitating fluid model results in a dramatically increased ice circulation as compared to the viscous-plastic model, and that the Mohr–Coulomb model has a behavior intermediate between these two cases. The increased ice transport is particularly pronounced in the Fram Straits outflow region between Greenland and Spitsbergen. It appears that this enhanced outflow is largely responsible for the somewhat lower ice volume in the cavitating fluid case discussed later.

Comparison of the cavitating fluid and viscous-plastic models over the entire 3-year simulation period is provided by the time series in Fig. 7. Figure 7a shows a monthly averaged time series of the average velocity magnitude in the Arctic basin for the two models for

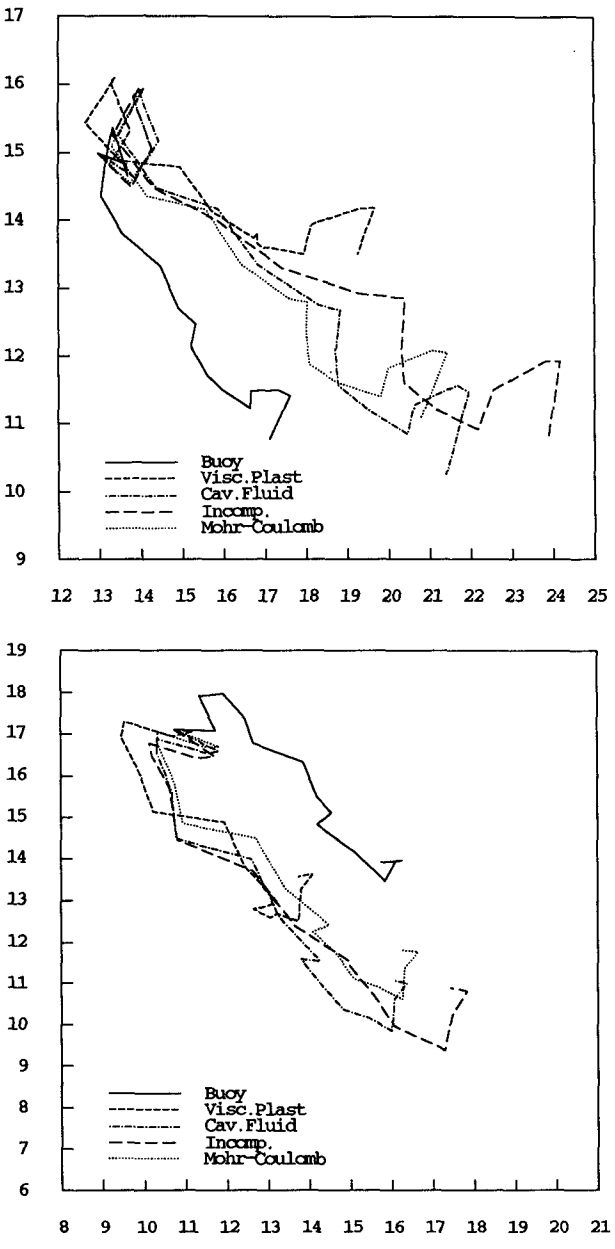

FIG. 9. Observed and computed buoy tracks for (a) buoy No. 3808 and (b) buoy No. 3809. Axes are labeled with computational grid indices; therefore, the tick mark spacing is 160 km.

TABLE 1.

Model	Buoy drift (km)	Model drift (km)	Error radius (km)
Viscous plastic	107.9	120.8	66.0
Cavitating fluid	107.9	146.6	74.1
Free drift	107.9	140.1	72.6
Incompressible	107.9	156.6	85.3
Mohr–Coulomb	107.9	139.0	65.2

both daily varying and monthly averaged wind forcing. During the summer months, when the ice strength is low, the two models produce similar average velocities (very close to free drift); however, during the high ice-strength winter period, the cavitating fluid model does not slow down nearly as drastically as the viscous-plastic model. This seasonal cycle is also reflected in the Fram Strait ice outflow time series in Fig. 7b. Over the entire simulation period using daily forcing, the average outflow for the viscous-plastic model was about 0.061 Sv (Sv $\equiv 10^6$ m^3 s^{-1}) as compared to 0.077 Sv for the cavitating fluid case (outflows for the monthly averaged wind case were 0.021 and 0.055 Sv, respectively). The Mohr–Coulomb model results are intermediate between the cavitating fluid and viscous-plastic results, however, the effect of the shear strength parameter, φ, has not been investigated. Figure 7 illustrates one of the most important features of the cavitating fluid model for climate applications; namely, the lack of shear strength allows a realistic ice circulation and outflow to be maintained even if smoothed wind forcing is used. The shear strength in the viscous-plastic case, on the other hand, provides more resistance than the relatively weak smoothed wind field can overcome and so motion virtually ceases.

It is instructive at this point to examine the model ice drift a little more closely and make some comparisons with observed ice drift. The Arctic Buoy Program maintains a number of data buoys on the Arctic ice cover, several of which were active during the 1981–83 period simulated here. Time series of the position of these buoys were provided by the Glaciological Data Center from data obtained by R. Colony (personal communication). Since the position of these buoys is reported on a daily basis (with some gaps), they provide a means of comparing observed ice drift to simulated drift in a manner similar to that of Hibler and Walsh (1982). Basically, the idea is to plot the position of the buoy at the beginning of each month to get a drift track for the buoy. A simulated drift track can be obtained by finding the monthly average model velocity at the buoy's midmonth position, multiplying by the number of seconds in the month to obtain a drift vector, and by plotting these vectors head to tail starting at the buoy's initial position. Note that this is not the same as a computed particle trajectory for a particle starting at the buoy's location but rather a means of presenting monthly drift vectors in a way that allows easy detection of consistent trends in the model velocity field.

To perform this comparison, six buoys were chosen (No. 3807, No. 3808, No. 3809, No. 3804, No. 3805, and No. 3814) that became operational in June 1981. The observed buoy drift tracks for these six buoys are shown in Fig. 8. The first three buoys were operational 17 or 18 months while the last three buoys were operational for 7 to 10 months. The monthly drift tracks shown in Figs. 9a,b allow a comparison of the various model drift tracks, including the free-drift and incompressible cavitating fluid models, for two buoy cases. Although the observed and computed drift tracks differ markedly in some cases, it must be remembered that even relatively small errors are magnified in this type of comparison if the errors have a consistent bias. It might be noted that over a long time period like this, consistent errors in the ocean currents may have a strong influence on the computed drift tracks. Since the ocean currents are represented here by the annual mean of a coupled ice–ocean model run with forcing from 1979 (Hibler and Bryan 1987), such errors may be the source of much of the error observed here. Comparison of a large number of buoys with a more complete coupled ice–ocean model would be a worthwhile study.

Some simple statistics allow a more objective comparison of the various models with observed buoy drift. Table 1 shows the average observed monthly drift along with the computed drift distance and the error radius (the magnitude of the vector difference between the observed and computed drift vectors). These results show that on average the viscous-plastic model exhibits drift magnitudes similar to those observed. This lends some more support to the ice-strength parameter, p^*, deduced by Hibler and Walsh (1982) based on the drift of a Russian ice station. The other models all show somewhat excessive drift with the incompressible cavitating fluid performing the worst.

Another measure of the performance of the various sea-ice models is provided by the correlation coefficients in Table 2. These correlation coefficients were calculated by considering the x and y components of the monthly buoy and model drift as complex time series [e.g., see Jenkins and Watts (1968) for the appropriate equations]. The results here indicate that

TABLE 2.

Model	Correlation coefficient
Viscous plastic	0.841
Cavitating fluid	0.829
Free drift	0.821
Incompressible	0.795
Mohr–Coulomb	0.852

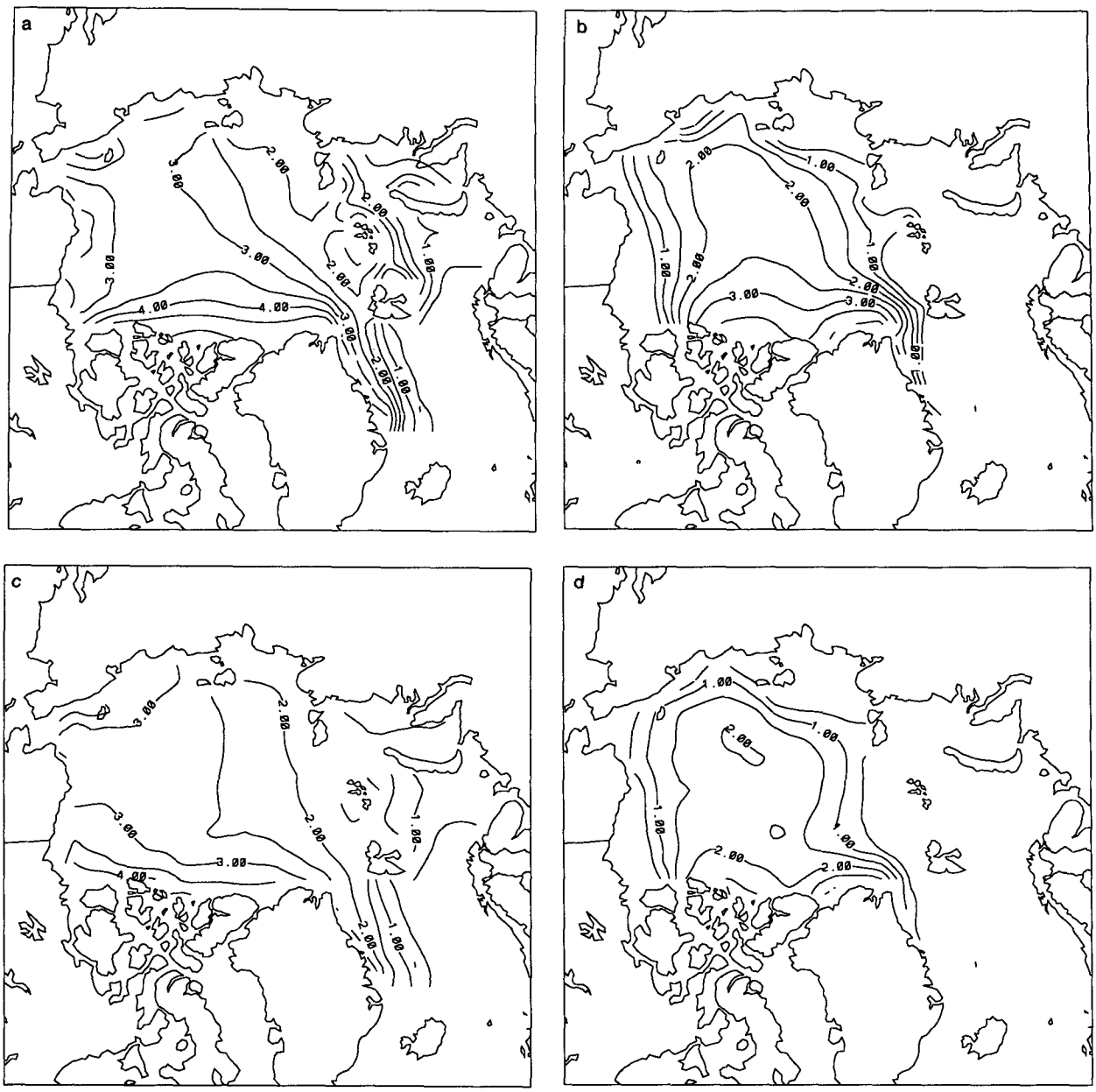

FIG. 10. Calculated thickness fields for 1983: (a) viscous plastic, March; (b) viscous plastic, August; (c) cavitating fluid, March; (d) cavitating fluid, August.

while all the models are well correlated with observed buoy drift, the two models that include a shear strength are significantly better correlated than those that do not. One thing that is clear from the above comparison is that correlation coefficients do not provide a particularly good measure of a model's overall performance; rather, it is the thickness buildup pattern that is most important. This is especially true in the case of the free-drift model wherein the drift correlation is not too different from the cavitating fluid or viscous-plastic models, yet the thickness buildup is completely unrealistic.

c. *Thickness buildup and ice edge comparisons*

The main reason for including a sea-ice dynamics model in large-scale climate studies is to allow the feedback between dynamics and thermodynamics via thickness buildup, lead formation, and ice transport. It is therefore of interest to examine the performance

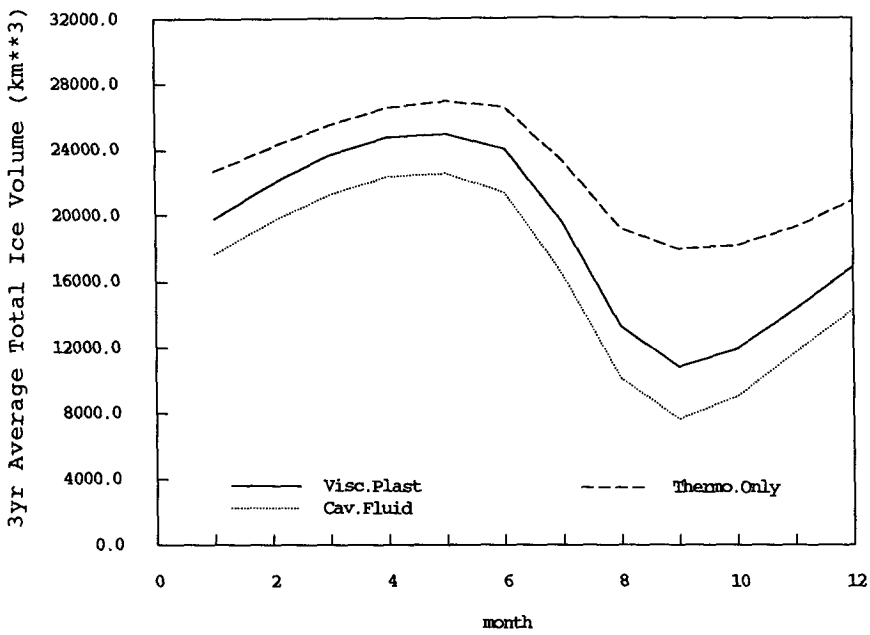

FIG. 11. Average seasonal cycle of total ice volume (km^3) for the viscous-plastic, cavitating fluid, and thermodynamics-only models.

of the cavitating fluid model by comparison with the viscous-plastic model and observations of the ice edge. The overall thickness buildup results are illustrated by the thickness fields for the end of March and August 1983 in Fig. 10. (The 1983 fields were chosen here to remove the effect of initial conditions on the thickness buildup.) Despite the differences in magnitude, the pattern of thickness buildup is broadly similar in both cases and generally agrees with that observed (e.g., see Bourke and Garrett 1987). In some places, the modeled ice thickness is perhaps a bit low, but natural variability (McLaren 1989) and the general paucity of data makes thickness comparisons difficult at this time. It is apparent from Fig. 10 that the ice in the Arctic basin is somewhat thinner in the cavitating fluid case, due primarily to the increased outflow through Fram Strait as discussed above. This can be modified substantially by adjusting the strength parameterization or by using smoothed wind forcing. The average seasonal cycle of ice volume in the Arctic basin over the 3-year simulation period is illustrated in Fig. 11. Also shown here is the ice volume calculated by a thermodynamics-only sea-ice model in which the thickness buildup pattern is roughly symmetrical around the pole (e.g., see Hibler and Walsh 1982). The effect of dynamics on the ice volume is twofold. First, the total volume is reduced by outflow, and second, the seasonal cycle is amplified due primarily to enhanced melting in summer caused by the formation of leads.

The position of the ice edge is an important climatic indicator that can be readily compared with model results as shown in Fig. 12. The observed ice edges were obtained from Walsh (personal communication) and represent the Naval Polar Oceanography Center's analyses, while the modeled ice edge is defined as the 20% compactness contour. The March ice edges computed by both models are very similar and are somewhat farther south than those observed. On the other hand, the ice edges computed for August are somewhat north of the observed positions, particularly in the cavitating fluid case. This is likely due to the generally thinner ice in the cavitating fluid simulation being more readily melted in summer. The fact that the simulated ice edges do not agree very well with those observed is not too surprising since the ice-edge position is dominated by heat flux from the ocean, which, in the models considered here, is a specified annual average value. To properly simulate the ice-edge position and, more importantly, its interannual variability, a coupled ice–ocean model is a necessity (Hibler and Bryan 1987).

The seasonal cycle of total ice area and lead area over the 3-year simulation period is shown in Fig. 13. The total ice area in Fig. 13a shows very little interannual variation as expected based on the preceeding discussion. The lead area in Fig. 13b (leads being defined as open water area in a grid cell with nonzero ice thickness) does show some seasonal variability since leads are formed primarily in response to wind patterns. Also interesting to note here is the somewhat larger lead area produced by the cavitating fluid model due

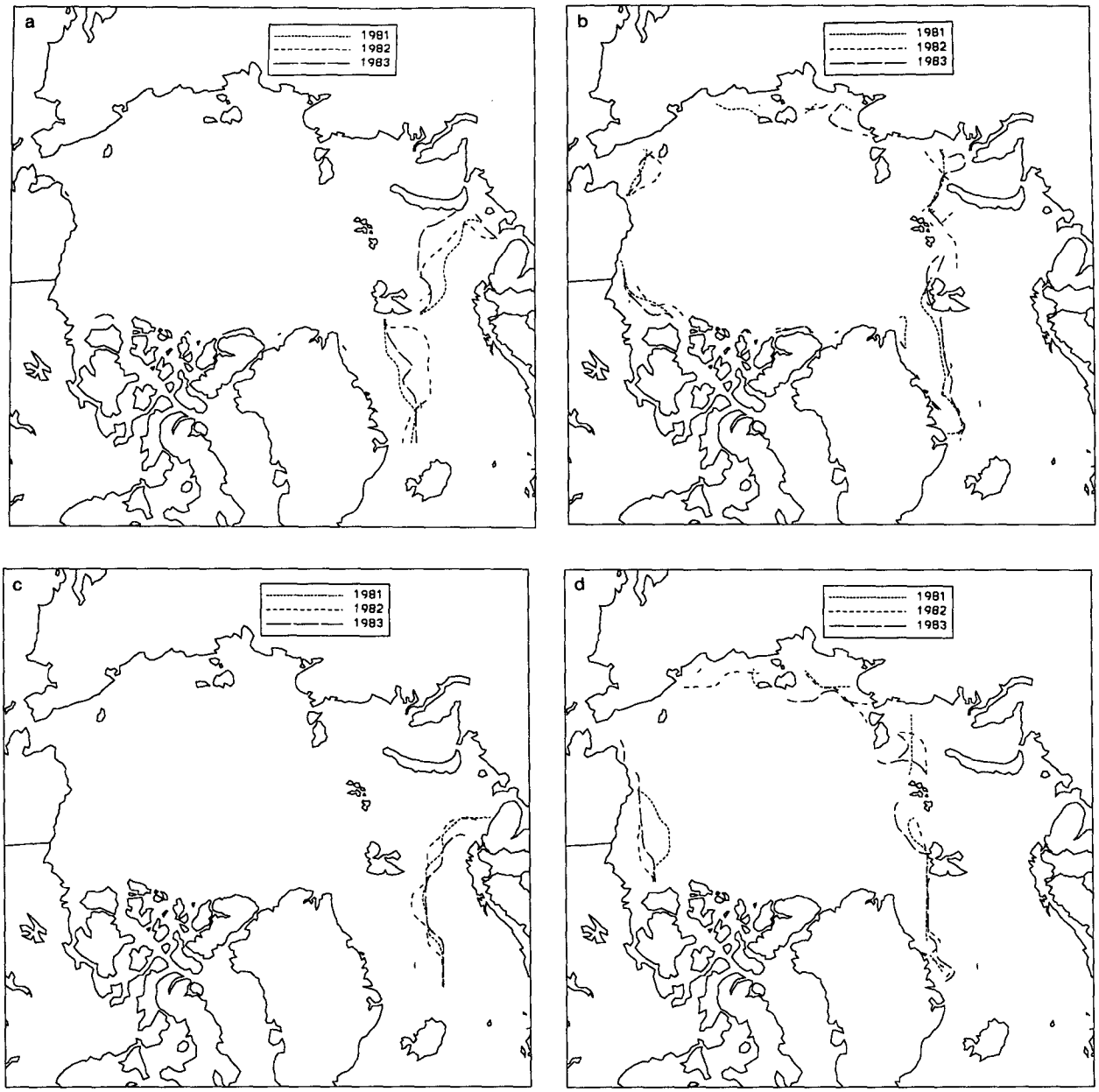

FIG. 12. Comparison of observed and calculated ice-edge position (defined as the 20% compactness contour) for (a) observed, March; (b) observed, August; (c) viscous plastic, March; (d) viscous plastic, August; (e) cavitating fluid, March; (f) cavitating fluid, August.

mainly to the more robust ice motion. We will return to this point in the next section as it relates to the calculated atmospheric heat flux.

d. Ice growth and heat flux

Polar pack ice plays an important role in moderating heat exchange between the atmosphere and ocean as well as providing a mechanism for lateral heat and salt transport. The impact of the cavitating fluid assumption on these processes will be discussed in this section along with some points about the influence of ice dynamics on long-term oceanic circulation patterns.

The net ice growth over the 3-year simulation period in Fig. 14 (shown as equivalent meters of ice growth) demonstrates that the cavitating fluid assumption has surprisingly little effect on the patterns of ice growth and decay. Note that the actual heat flux to the atmosphere is augmented by the specified oceanic heat flux in areas with no ice; however, the net growth

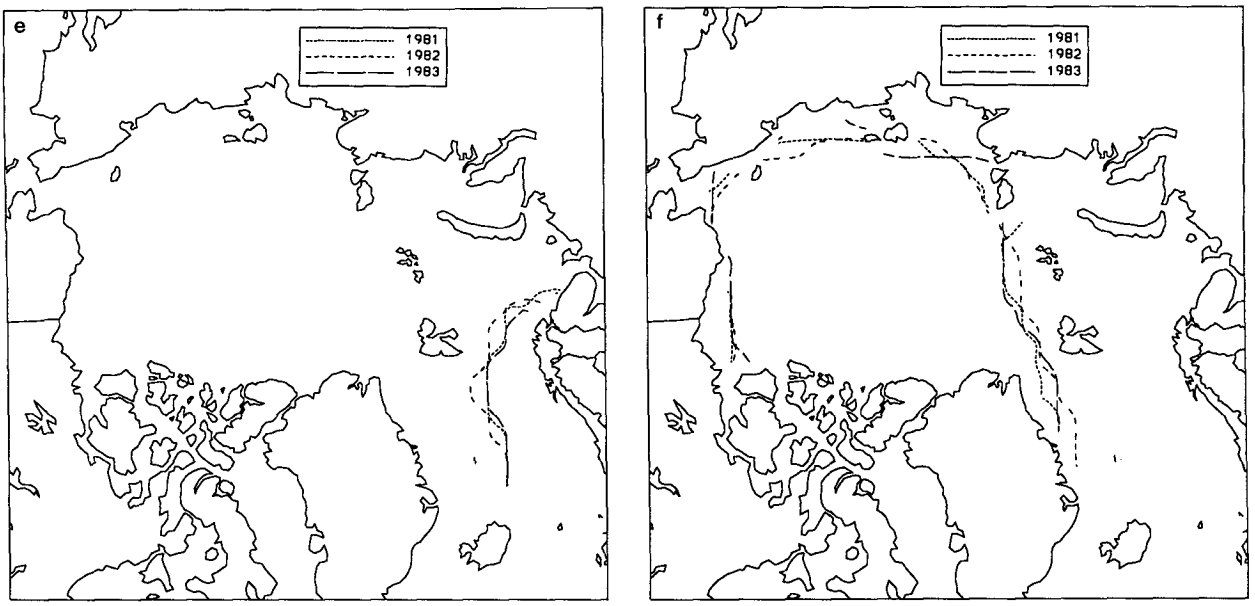

FIG. 12. (*Continued*)

translates directly into salt flux to the ocean. The dashed contours in the figure represents areas where there was net ice melt over the year—solid lines represent net ice growth. It is interesting that there was very little seasonal variability of this pattern over the 3-year simulation period, and so the patterns shown in Fig. 14 represent rather consistent trends. Of particular note are the areas of net melt in the Beaufort and East Siberian seas (indicating a net transport of ice into these regions and a concomitant freshwater flux) and the prominant areas of net ice growth in the Laptev and Kara seas (indicating a net efflux of ice from these areas and a salt flux into the ocean). Also visible is the net ice melt in the Greenland Sea as the ice flowing out through Fram Strait encounters the large oceanic heat flux in this region.

These patterns of ice growth and melt and the concomitant salt fluxes are perhaps the most important reason for including sea-ice dynamics in long-term studies of climate and global change. The important feedback effect of ice transport on oceanic circulation is neglected if only the thermodynamic behavior of the ice cover is modeled.

The overall seasonal behavior of the heat transfer from the Arctic basin to the atmosphere is illustrated by the 3-year average heat transfer plot in Fig. 15a. This plot also contains the thermodynamics-only model for comparison. The larger seasonal cycle in the two models that include dynamics is due to the large heat flux through leads. This point is further illustrated by the plot of heat transfer through leads only in Fig. 15b. The larger seasonal swing in the cavitating fluid case is due to the larger lead area discussed earlier, which accentuates both melting and freezing. It is interesting that on a cumulative basis, the atmosphere experiences a net gain of heat from leads in the viscous-plastic model and a net loss to leads in the cavitating fluid model; however, this is almost exactly countered by the increased growth of the generally thinner ice in the cavitating fluid case so that, overall, the total heat flux to the atmosphere is about the same in both cases.

4. Linear drag, spherical coordinates, and islands

A quadratic drag formulation requires a two-step time-stepping scheme such as that described in section 2. A linear drag formulation eliminates this requirement and thus almost halves the computational effort. In this case, only Eq. (15a) is used to step the velocity forward in time (with κ + replaced by κ + 1). The wind- and water-drag coefficients in (2) and (3) used in the linear-drag formulation are $C_a^* = 0.01256$ and $C_w^* = 0.6524$, respectively.[3] This linear drag, cavitating fluid model is the same as that used by Flato and Hibler (1990) except that the Arakawa C grid is used here. Figure 16 shows the March 1983 thickness field calculated by the linear drag, rectangular grid model and can be compared to Fig. 10b. The effect of simplifying the drag parameterization is to reduce the buildup against the Canadian archipelago slightly. The difference is not too great and can likely be tolerated for

[3] These coefficients were obtained by averaging the daily nonlinear drag coefficients over the entire Arctic basin for a year (Flato and Hibler 1990).

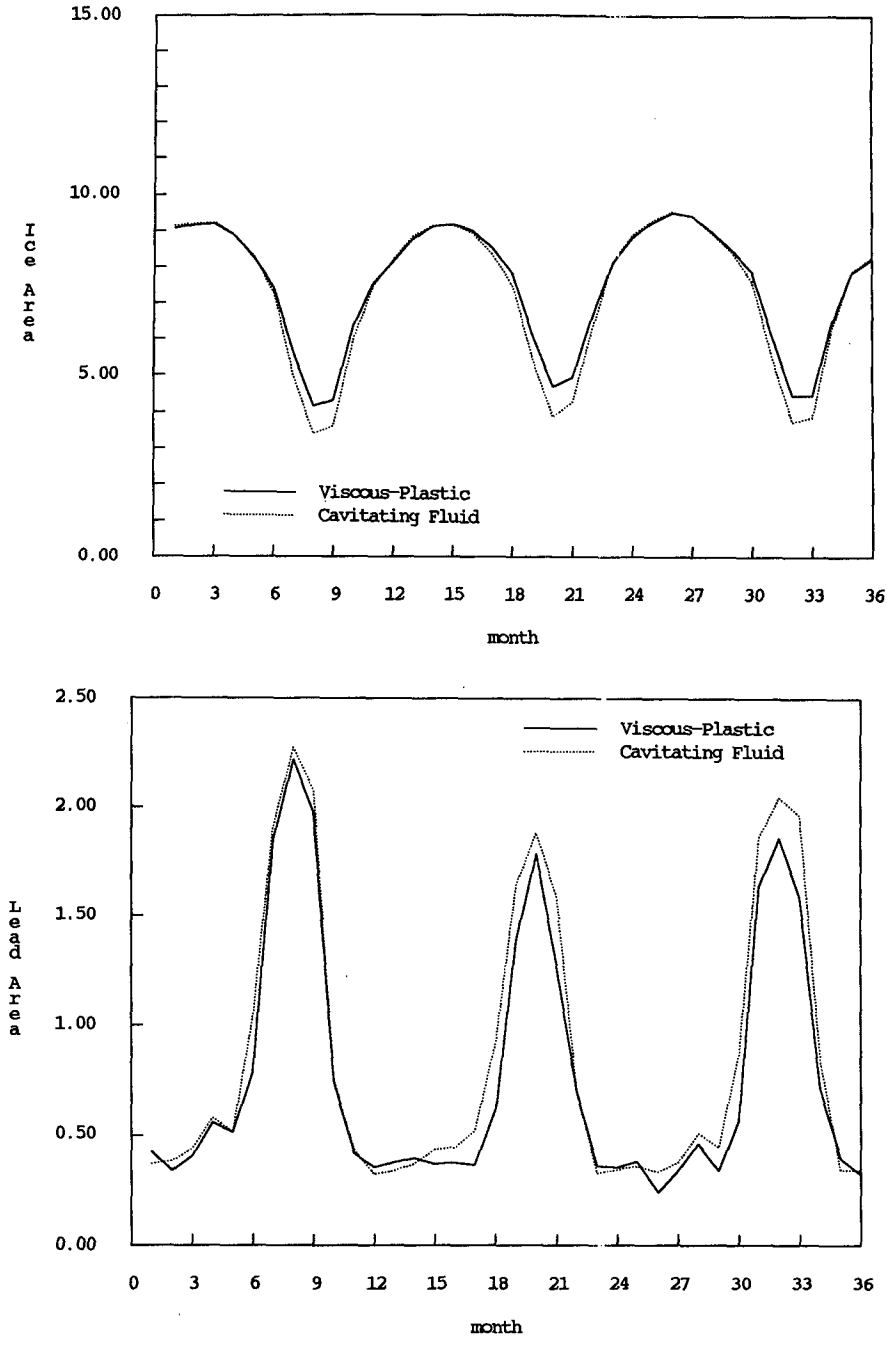

FIG. 13. Time series of (a) area covered by ice and (b) area covered by leads (defined as open-water area in a grid cell with nonzero ice thickness) in units of 10^6 km^2.

climate modeling purposes in return for almost doubling the computational speed.

While the rectangular grid model is useful for basin-scale studies, a spherical grid is necessary in most large-scale climate simulations. Figure 17 shows the grid configuration for such a model in which the grid spacing is 2° lat by 10° long. The cavitating fluid scheme is useful in this case, not only when simplicity and speed are important, but also when an artificial island is used to eliminate the singularity at the pole. Shear resistance in a more complete sea-ice rheology would cause a severe restriction in ice outflow from the basin and result in undesirable thickness buildup around the artificial polar island, a fact confirmed by rectangular

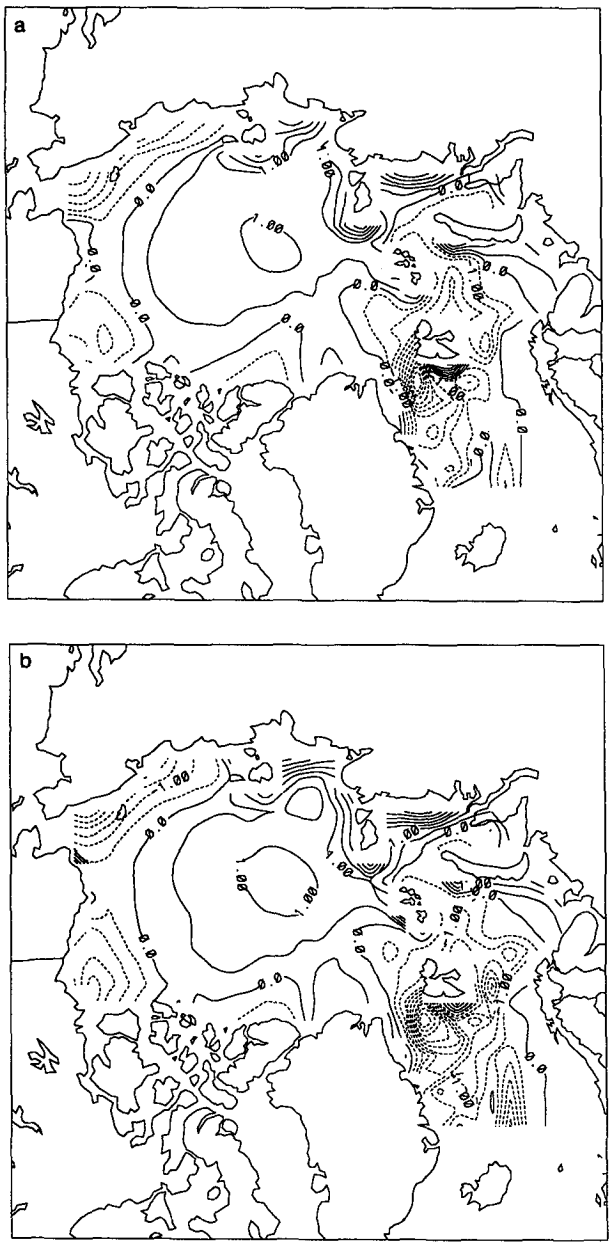

FIG. 14. Contours of net ice growth over 3-yr simulation period: (a) viscous-plastic model; (b) cavitating fluid model. Contour interval is 0.5 m and dashed lines represent negative values (i.e., regions of net melt).

grid simulations. Some results will also be shown for a spherical grid version of the model that does not have an island at the pole, in which case the circular region near the pole is treated as a special grid cell.

The spherical grid version of the cavitating fluid model was developed using the equations described in appendix B and the aforementioned linear wind and water-drag formulations. Except for the change to spherical coordinates, the model equations and implementation are identical to the rectangular grid case and so will not be repeated here. A complete documentation of the linear drag, spherical grid model is available to supplement the description provided in this paper (Flato 1991). The same forcing fields as in the rectangular grid case were used here and were simply interpolated to the spherical grid assuming an azimuthal equidistant projection.

The velocity and thickness fields in Fig. 18 for the model with an island at the pole show that although the island presents an obstruction to the flow, the lack of shear strength allows the ice to slip cleanly around the obstruction with no local irregularities in the thickness field. The spherical grid model with an island at the pole will likely be useful in conjunction with large-scale oceanic circulation models, which use an artificial island to avoid the mathematical singularity at the pole. Atmospheric general circulation models, on the other hand, have ways of handling the polar singularity, and so, an ice model with an island is not as desirable in this case. The mathematical simplifications that arise from neglecting shear strength in the cavitating fluid model allow the island to be replaced with a special circular grid cell so that continuous thickness and velocity fields can be computed near the pole.

The March 1983 thickness field calculated by the spherical grid model with no island is shown in Fig. 19a and it differs little from that calculated by the model with an island, confirming the finding that the cavitating fluid model is affected little by this artificial obstruction. In both cases the monthly average velocity field is very similar to that found in the rectangular grid case, and the difference imposed by the artificial polar island can only be seen when the velocity fields are superimposed. Some differences do exist between the rectangular and spherical grid thickness fields. This is attributed mainly to the spatial smoothing of the wind field during interpolation to the cruder resolution spherical grid.

The outflow through Fram Strait calculated by the two spherical grid models is compared to the rectangular grid model in Fig. 20. The spherical grid models differ little as expected from the above comparison of the flow patterns and are in general agreement with the rectangular grid model. The rectangular and spherical grids only differ substantially in fall. This is a result of using upstream differencing for advection, which combines with the rather crude resolution in the spherical grid case to keep the ice edge somewhat farther south and hence allows substantial ice outflow to begin earlier in the season.

5. Conclusions

The cavitating fluid rheology assumes that sea ice has a compressive strength only and no resistance to divergence or shear. This rheology and several attempts at implementing it have been presented by others in

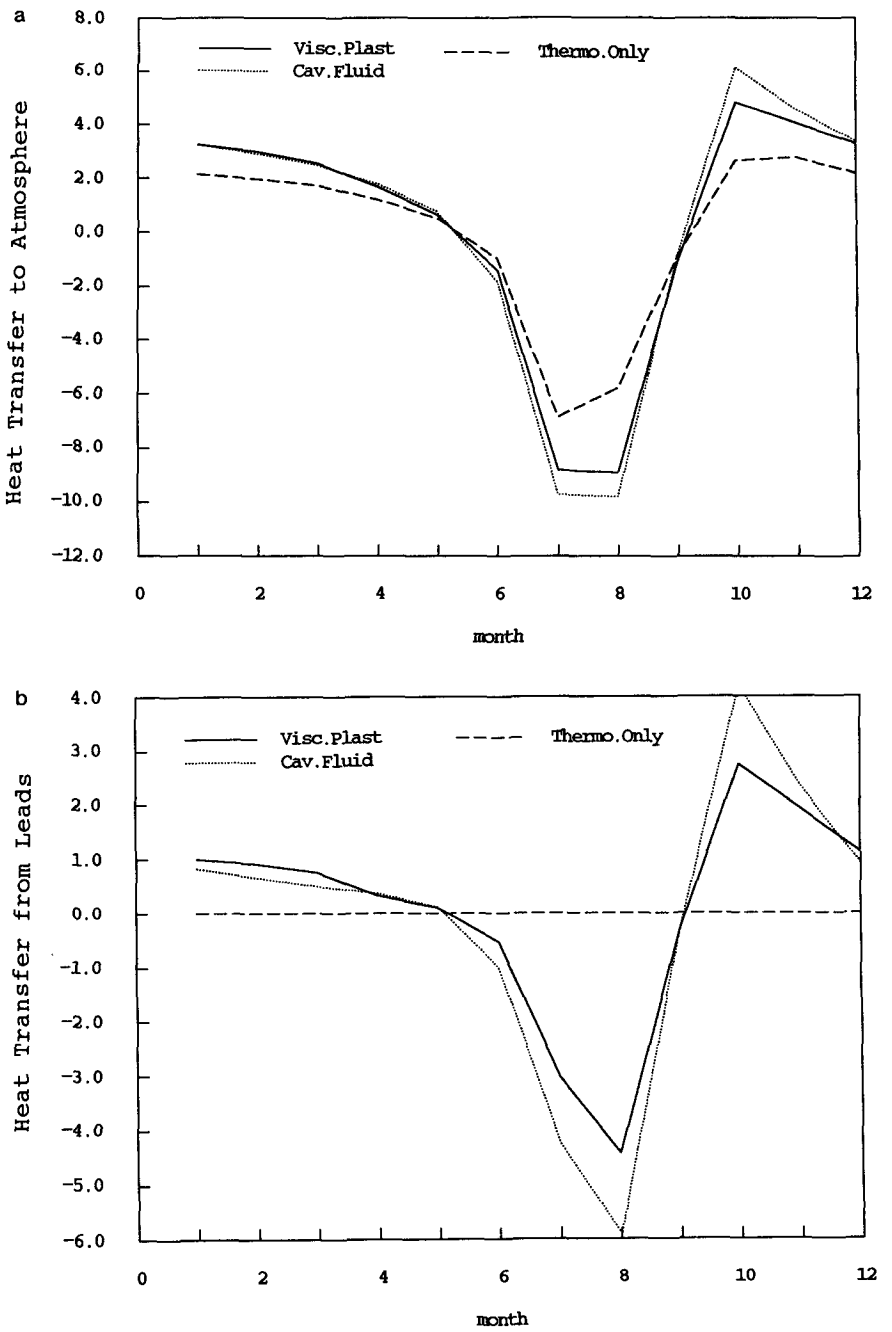

FIG. 15. Average seasonal cycle of heat transfer to the atmosphere over the Arctic basin in equivalent meters of ice per year for the viscous-plastic, cavitating fluid, and thermodynamics-only models (1 m of ice per year is equivalent to 9.58 W m^{-2}): (a) total heat transfer; (b) heat transfer from leads only.

the past. The contribution of the present paper is a simple, consistent numerical procedure based on successive corrections to the pressure and velocity fields. The Arakawa C-grid formulation was found to be superior to the B grid due the the smoother pressure fields produced when incompressible flow is to be modeled; otherwise, the two grid schemes produce almost identical results. The strength of the numerical scheme presented here is its ease of implementation in either rectangular or spherical coordinates and its computational

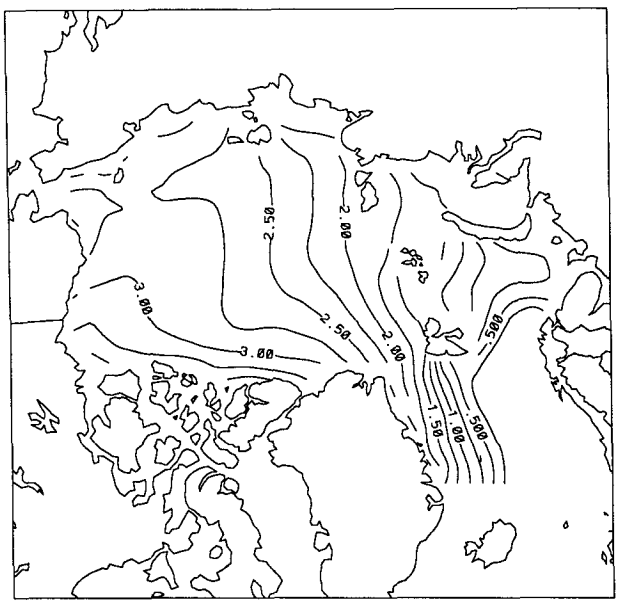

FIG. 16. Thickness field for March 1983 calculated by the linear drag, rectangular grid cavitating fluid model. Contour interval is 0.5 m.

efficiency when compared to a direct time-stepping integration (Semtner 1987; Ip et al. 1991).

A number of comparisons were made to the more complete viscous-plastic rheology of Hibler (1979) by conducting simulations of the entire Arctic ice cover with real forcing from 1981 to 1983. These simulations

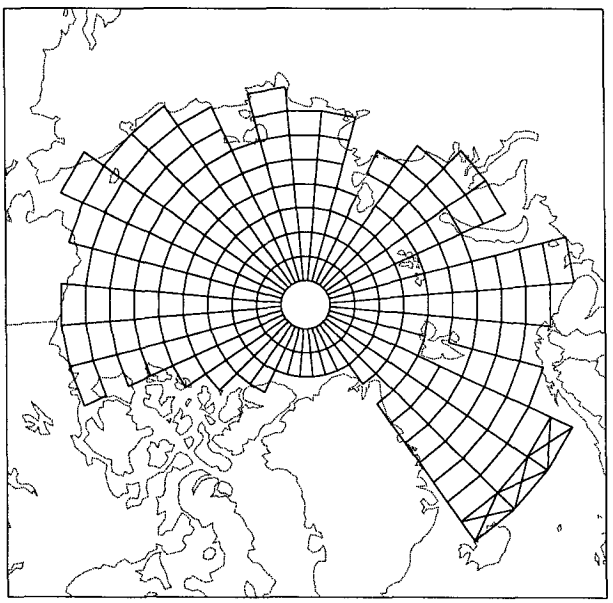

FIG. 17. Computational grid for spherical coordinate version of cavitating fluid model. Grid spacing is 2° lat and 10° long. Cross-hatched grid cells indicate outflow boundary conditions.

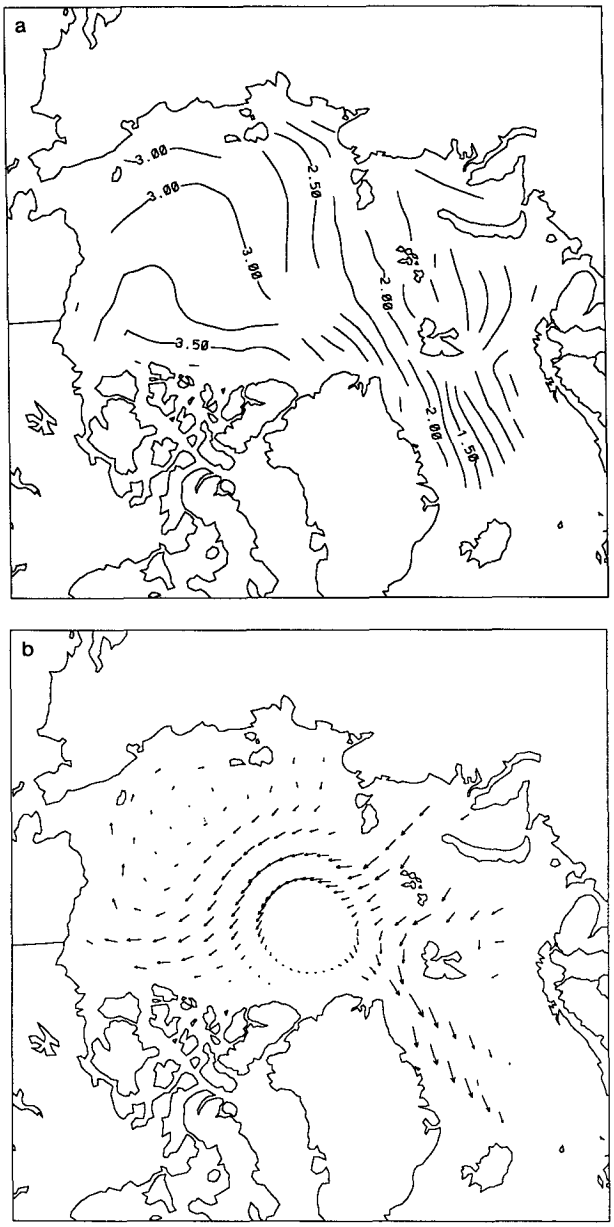

FIG. 18. Thickness and velocity fields for March 1983 calculated by spherical grid cavitating fluid model with an artificial island at the pole: (a) thickness field, contour interval of 0.25 m; (b) velocity field, vectors are plotted to the same scale as the rectangular grid results in Fig. 6 to allow direct comparison.

showed that while the lack of shear strength in the cavitating fluid rheology increased the ice outflow through the Fram Strait and the average Arctic basin ice velocity in winter, the heat flux to the atmosphere and ice-edge position were affected very little. The enhanced outflow in the cavitating fluid case resulted in about 10% less ice volume in the Arctic basin, however, the pattern of thickness buildup differed little from the viscous-plastic case. A limited comparison of modeled and ob-

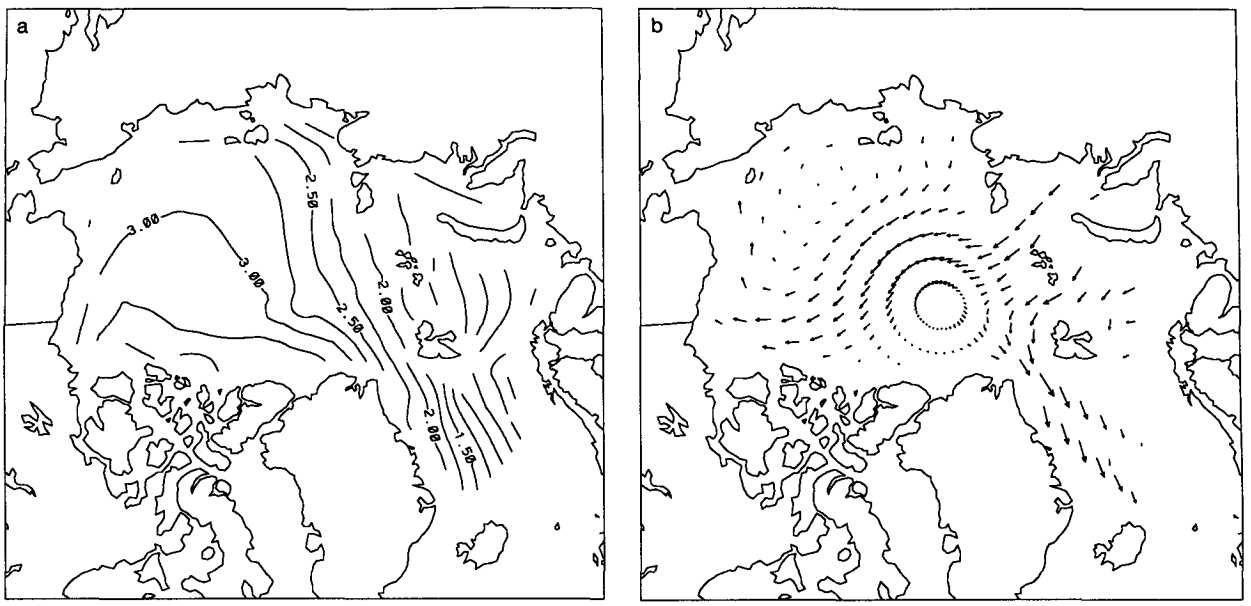

FIG. 19. Thickness and velocity fields for March 1983 calculated by spherical grid cavitating fluid model with no island at the pole: (a) thickness field, contour interval of 0.25 m; (b) velocity field, vectors are plotted to the same scale as the rectangular grid results in Fig. 6.

served buoy drift was also conducted, which showed that while drift of the viscous-plastic, cavitating fluid, Mohr–Coulomb, and free-drift models all correlated well with observed monthly drift, the models that included shear strength correlated somewhat better. The excessive drift in the cavitating fluid and Mohr–Coulomb models could likely be reduced by appropriate tuning of either the strength parameterization or drag

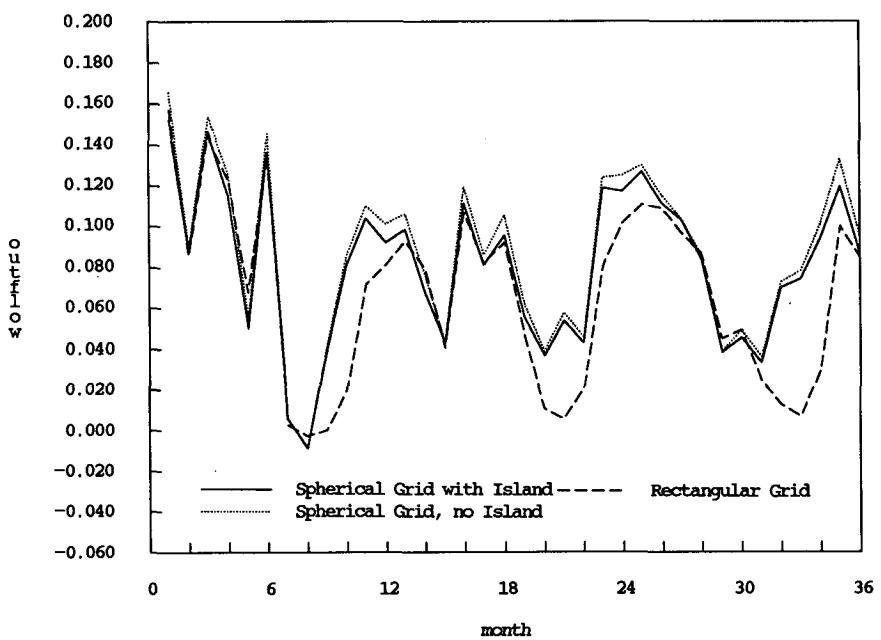

FIG. 20. Time series of monthly average ice outflow through Fram Strait (in Sverdrups) for the two versions of the spherical grid model and a linear drag, rectangular grid version of the cavitating fluid model for comparison.

coefficients; however, this robust circulation was found to be useful in cases where the wind field was smoothed by time averaging.

A spherical grid implementation demonstrated another useful characteristic of the cavitating fluid rheology by producing reasonable ice thickness buildup even with a large artificial island placed at the pole to avoid the mathematical singularity. It is the lack of shear strength that allows free slip past an obstruction, which would otherwise give rise to pronounced thickness buildup. An extension of the spherical grid model that replaces the artificial island with a special circular grid cell to avoid the polar singularity was also discussed, with results that differed little from the island case.

Overall, the cavitating fluid rheology and the numerical scheme presented here offer considerable promise as a sea-ice parameterization in long-term, crude resolution climate investigations with global atmospheric or oceanic circulation models due to its simplicity and its ability to reproduce the dynamic–thermodynamic feedback of a more complete sea-ice model. The cavitating fluid model is less suited to detailed studies of local ice drift where shear strength may be important; however, the pressure field calculated by the incompressible version of the model may be useful in some contexts and an extension of the numerical scheme to allow inclusion of a realistic shear strength, via a nonlinear shear viscosity, is relatively straightforward.

APPENDIX A

Comparison of B-grid and C-grid Formulations

The Arakawa B-grid finite-difference formulation is often used in large-scale sea-ice, ocean, and atmospheric circulation models because of certain energy-conserving properties (Bryan 1969). One drawback to this scheme is that the finite-difference form of the Laplacian of a scalar field is insensitive to alternating gridpoint or "checkerboard" wave patterns superimposed on the true field. In cases of truly divergence-free flow, this does not pose a problem for the pressure field because it is not explicitly used in the calculations; the common trick of taking the curl of the momentum equation to eliminate the gradients of scalar functions and computing the streamfunction rather than the velocity field assures this. In the present case the pressure field is a vital part of the calculation and it appears in a Laplacian-like equation (10).

The Arakawa B-grid used by Flato and Hibler (1990) was found to exhibit the aforementioned alternating gridpoint wave pattern when incompressible flow was modeled, although the effect was barely perceptible in cases with a finite compressive strength. The Arakawa C-grid is often used in cases where the pressure field must be treated explicitly (e.g., tidal models) and has proven effective in suppressing this alternating gridpoint oscillation. What is apparent is that the overall pressure-field pattern in the B-grid case is very similar to the C-grid case, and so it appears that there may be simply a wave pattern superimposed on the "correct" pressure field. If a finite compressive strength is allowed, much of the oscillation is removed. Indeed the Arctic basin pressure and thickness buildup results for the two versions of the model during year 3 of a simulation using climatology forcing (Fig. A1) are very similar, and so the alternating gridpoint oscillation may be merely an annoyance.

APPENDIX B

Spherical Coordinate Formulation

a. Finite difference scheme with island at pole

In a spherical coordinate, Arakawa C-grid cell such as that shown in Fig. B1, the divergence in finite-difference form is given by

$$\nabla \cdot \mathbf{u} = \frac{1}{R \cos\phi_{j+1/2}} \left[\frac{1}{\Delta\lambda} (u_{i+1,j} - u_{i,j}) + \frac{1}{\Delta\phi} (v \cos\phi_{i,j+1} - v \cos\phi_{i,j}) \right] \quad \text{(B1)}$$

where R is the radius of the earth, ϕ is the latitude, λ is the longitude, and u and v are the longitudinal and latitudinal components of the velocity. Following the same derivation as for the rectangular case discussed in the main text, the pressure correction is given by

$$\tilde{p}_{i+1,j+1} = -(\nabla \cdot \mathbf{u}) R^2 \cos\phi_{j+1/2} \Big/ \left\{ \frac{1}{\Delta\lambda^2} \left[\frac{1}{\alpha^x_{i+1,j} \cos\phi_{j+1/2}} + \frac{1}{\alpha^x_{i,j} \cos\phi_{j+1/2}} \right] + \frac{1}{\Delta\phi^2} \left[\frac{\cos\phi_{j+1}}{\alpha^y_{i,j+1}} + \frac{\cos\phi_j}{\alpha^y_{i,j}} \right] \right\} \quad \text{(B2)}$$

and the velocity corrections by

$$\tilde{u}_{i,j} = \frac{-1}{\alpha^x_{i,j} R \cos\phi_{j+1/2}} \frac{\tilde{p}_{i+1,j+1}}{\Delta\lambda}$$

$$\tilde{u}_{i+1,j} = \frac{1}{\alpha^x_{i+1,j} R \cos\phi_{j+1/2}} \frac{\tilde{p}_{i+1,j+1}}{\Delta\lambda}$$

$$\tilde{v}_{i,j} = \frac{-1}{\alpha^y_{i,j} R} \frac{\tilde{p}_{i+1,j+1}}{\Delta\phi}$$

$$\tilde{v}_{i,j+1} = \frac{1}{\alpha^y_{i,j+1} R} \frac{\tilde{p}_{i+1,j+1}}{\Delta\phi} . \quad \text{(B3)}$$

The correction scheme proceeds exactly as in the rectangular case, except that several relaxation sweeps must be made through the grid cell rows nearest the

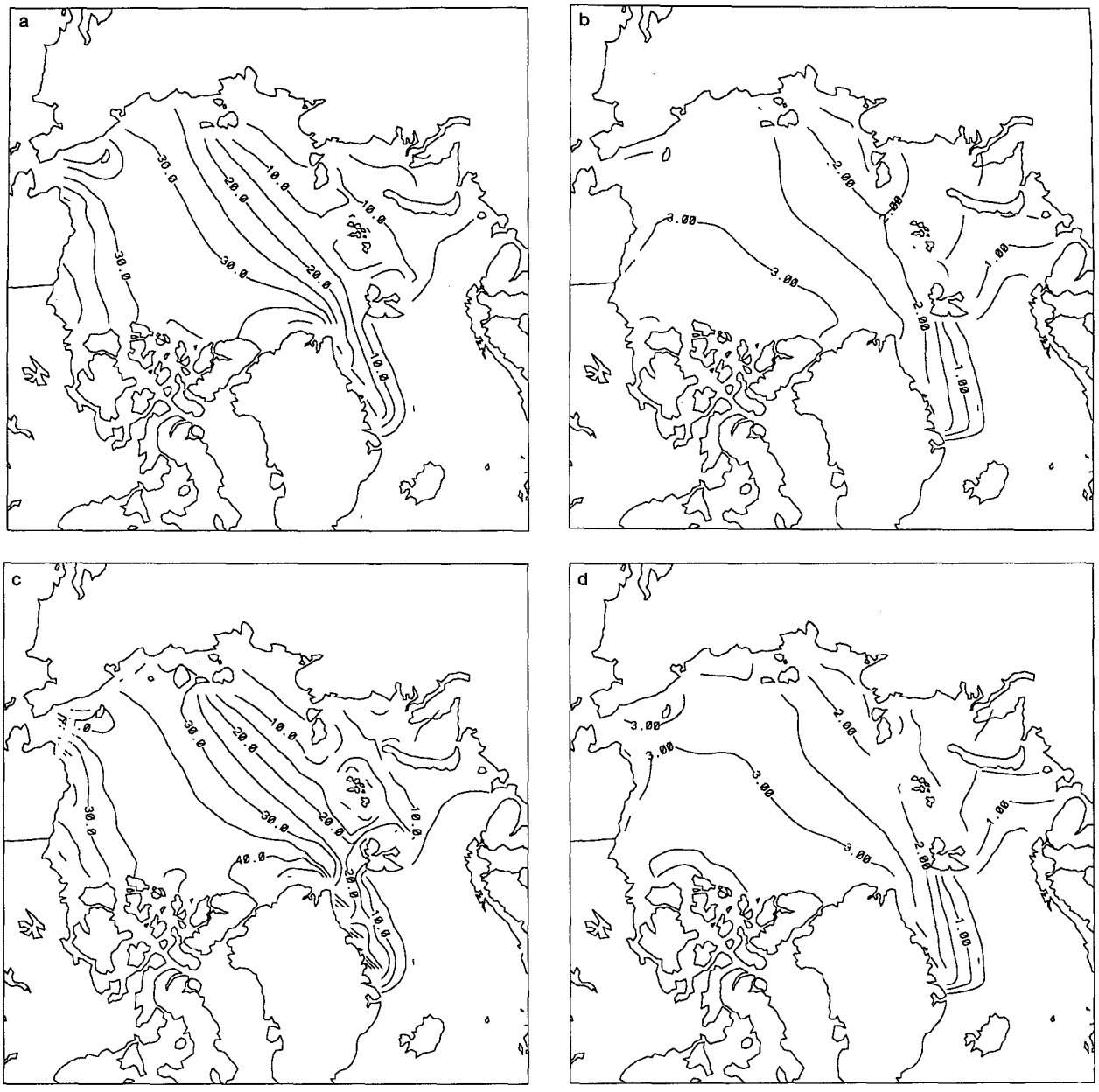

FIG. A1. Comparison of pressure and thickness fields for March 1983 calculated by C-grid and B-grid versions of the cavitating fluid model: (a) C-grid pressure field; (b) C-grid thickness field; (c) B-grid pressure field; (d) B-grid thickness field. Contour intervals are 5 kN m^{-1} and 0.5 m.

pole for every sweep through the entire grid. The reason for this is the relatively small change in meridional velocity imposed by a pressure perturbation in the narrow grid cells near the pole and the concomitant slow convergence of the relaxation scheme in this region.

b. Finite-difference scheme with no island at pole

The polar grid cell is sketched in Fig. B2 with the meridional velocities all shown as positive. Although the divergence rate at the pole is not really defined mathematically it is obvious that the appropriate definition for our purposes is

$$\mathrm{div}_{\mathrm{pole}} = -\sum_{i=1}^{N} v_{i,M} \qquad \text{(B4)}$$

where N is the number of longitude divisions and M is the subscript for the latitude of the polar grid-cell boundary. Having made this definition, the remainder

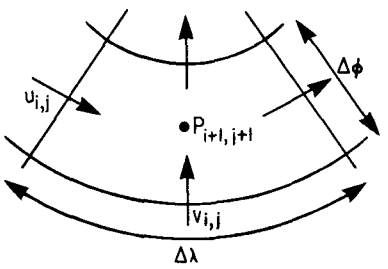

FIG. B1. Computational grid cell for spherical grid version of model showing location of vector and scalar quantities.

of the correction scheme is identical to the regular grid cells. The individual velocity corrections are essentially the same as those given above, namely,

$$\tilde{v}_{i,M} = \frac{-1}{\alpha^{y}_{i,M} R} \frac{\tilde{p}_{\text{pole}}}{\Delta\phi} \tag{B5}$$

where $\tilde{p}_{\text{pole}}$ is the pressure correction applied to the polar grid cell. The value of $\tilde{p}_{\text{pole}}$ required to make the divergence zero is

$$\tilde{p}_{\text{pole}} = R\Delta\phi \frac{\sum_{i=1}^{N} v_{i,M}}{\sum_{i=1}^{N} \frac{1}{\alpha^{y}_{i,M}}}. \tag{B6}$$

For the simulation results below, the same grid configuration was used as in the case with an island at the pole resulting in an oversized grid cell at the pole. This is readily handled by using a different value of $\Delta\phi$ for the corrections in Eqs. (B5) and (B6) than in the corrections to the normal grid cells. Advection is handled in a straightforward manner with the change in thickness in the polar grid cell calculated from the sum of the fluxes across all of the boundary segments.

APPENDIX C

Extension of Cavitating Fluid Scheme to Include Shear Strength via Mohr–Coulomb Failure Criteria

The cavitating fluid rheology with its lack of shear strength has some advantages for including sea-ice dynamics in climate models, as the results in the main body of the text show. However, the numerical scheme to implement the cavitating fluid rheology can be extended somewhat to include shear strength if desired. The basic idea is to split the internal ice-stress tensor into two parts: a pressure term calculated by the cavitating fluid scheme and a shear term calculated using a nonlinear shear viscosity and the differencing scheme developed by Ip et al. (1991). The shear viscosities are chosen as in the Hibler (1979) viscous-plastic model such that either the stress state satisfies a plastic yield criterion or the deformation rate is negligibly small. However, the normal-flow rule and elliptical yield curve used by Hibler (1979) are replaced here by a Mohr–Coulomb failure criterion.

Introducing a shear viscosity, the ice interaction term, **F**, in Eq. (1) is given by

$$\mathbf{F} = \nabla \cdot \sigma_{ij} \tag{C1}$$

$$\sigma_{ij} = 2\eta(\dot{\epsilon}_{ij}, p)\dot{\epsilon}_{ij} - \eta(\dot{\epsilon}_{ij}, p)\dot{\epsilon}_{kk}\delta_{ij} - p\delta_{ij} \tag{C2}$$

where σ_{ij} is the two-dimensional stress tensor, $\dot{\epsilon}_{ij}$ is the strain rate tensor, η is the nonlinear shear viscosity described below (an explicit function of $\dot{\epsilon}_{ij}$ and p), and δ_{ij} is the Kroneker delta function. Carrying out the differentiation in (C1) and writing the strain rate in terms of velocity gradients, the x component of **F** is given by

$$F_x = -\frac{\partial p}{\partial x} + \frac{\partial}{\partial x}\left[\eta\left(\frac{\partial u}{\partial x} - \frac{\partial v}{\partial y}\right)\right] + \frac{\partial}{\partial y}\left[\eta\left(\frac{\partial u}{\partial y} + \frac{\partial v}{\partial x}\right)\right]. \tag{C3}$$

The last two terms in (C3) have the following finite-difference form

$$\frac{\partial}{\partial x}\left[\eta\left(\frac{\partial u}{\partial x} - \frac{\partial v}{\partial y}\right)\right] = \frac{1}{\Delta x}\eta_{i+1,j+1}\left[\frac{u_{i+1,j} - u_{i,j}}{\Delta x} - \frac{v_{i,j+1} - v_{i,j}}{\Delta y}\right] - \frac{1}{\Delta x}\eta_{i,j+1}\left[\frac{u_{i,j} - u_{i-1,j}}{\Delta x} - \frac{v_{i-1,j+1} - v_{i-1,j}}{\Delta y}\right] \tag{C4}$$

$$\frac{\partial}{\partial y}\left[\eta\left(\frac{\partial u}{\partial y} + \frac{\partial v}{\partial x}\right)\right] = \frac{1}{4\Delta y}(\eta_{i+1,j+1} + \eta_{i,j+1} + \eta_{i,j+2} + \eta_{i+1,j+2})\left[\frac{u_{i,j+1} - u_{i,j}}{\Delta y} + \frac{v_{i,j+1} - v_{i-1,j+1}}{\Delta x}\right]$$
$$- \frac{1}{4\Delta y}(\eta_{i+1,j+1} + \eta_{i,j+1} + \eta_{i,j} + \eta_{i+1,j})\left[\frac{u_{i,j} - u_{i,j-1}}{\Delta y} + \frac{v_{i,j} - v_{i-1,j}}{\Delta y}\right]. \tag{C5}$$

The y component is obtained in an analogous manner. Note that the shear viscosities are defined at the same grid locations as the thickness and pressure.

The shear viscosities are chosen at each location such that either the Mohr–Coulomb yield criterion is satisfied or the deformation rate is negligibly small (i.e.,

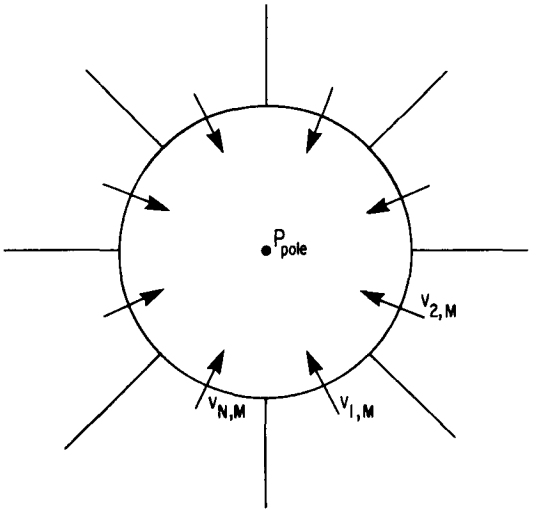

FIG. B2. Special polar grid cell for spherical grid version of model with no artificial island at pole. Indicies n and m refer to the zonal and meridional location in the grid with N being the number of grid cells in the zonal direction and M the number of grid cells in the meridional direction.

a small amount of viscous creep is used to approximate rigid behavior). The Mohr–Coulomb yield criterion is commonly used in soil mechanics and is simply a linear relationship between the shear and normal stress at failure. In the sea-ice case, the pressure is limited by the assumed compressive strength, and so the Mohr–Coulomb failure surface does not extend to infinity but rather has a "cap" as shown in Fig. 4. Mathematically, this yield condition is given by

$$(\sigma_1 + \sigma_2)\sin\varphi = (\sigma_1 - \sigma_2) \qquad \text{(C6)}$$

where φ is a parameter, the so-called angle of internal friction. Note that $p = (\sigma_1 + \sigma_2)/2$ and since the principal stress and strain directions are assumed to coincide, the appropriate shear viscosity is given by

$$\eta = \min\left\{\frac{p\sin\varphi}{\dot{\epsilon}_1 - \dot{\epsilon}_2}, \eta_{\max}\right\} \qquad \text{(C7)}$$

where $\eta_{\max}$ is a specified maximum viscosity that determines the point at which the shear strain rate is negligibly small.

Now, given a pressure field calculated by the cavitating fluid scheme, the shear viscosities at every point in the grid are determined by Eq. (C7). The velocity field satisfying the equation of motion (1) can be found by relaxation, taking the diagonal terms in (C4) and (C5) to the left-hand side of the equation. Of course the resulting velocity field will not necessarily satisfy the cavitating fluid conditions relating pressure to divergence rate, and so one might wish to iterate a few times to get a solution that satisfies both the cavitating fluid conditions and the Mohr–Coulomb conditions. In the simulation results discussed in the main body of the paper, the shear and pressure correction schemes were repeated twice for both steps in the modified Euler time step with $\eta_{\max} = 10^{12}$ and $\varphi = 24°$.

Acknowledgments. We would like to thank C. F. "Billy" Ip for performing the direct time-stepping calculations and James Waugh and Peter Ranelli for their assistance with the NCAR graphics used to produce the vector and contour plots. The forcing fields were interpolated from their original form by Jin Lun Zhang. This work was supported by the Office of Naval Research under Contract N00014-86-K-069.

REFERENCES

Bourke, R. H., and R. P. Garrett, 1987: Sea ice thickness distribution in the Arctic Ocean. *Cold Reg. Sci. Technol.*, **13,** 259–280.

Bryan, K., 1969: A numerical method for the study of the circulation of the world oceans. *J. Comput. Phys.*, **4,** 347–376.

——, S. Manabe, and R. L. Pacanowski, 1975: A global ocean–atmosphere climate model. Part II. The Oceanic Circulation. *J. Phys. Oceanogr.*, **5,** 30–46.

Coon, M. D., G. A. Maykut, R. S. Pritchard, D. A. Rothrock, and A. S. Thorndike, 1974: Modeling the pack ice as an elastic–plastic material. *AIDJEX Bull.*, **24,** 1–105.

Crutcher, H. L., and J. M. Meserve, 1970: Selected level heights, temperatures and dew points for the Northern Hemisphere, NAVAIR 50-IC-52, Naval Weather Service Command, Washington, D.C.

Flato, G. M., 1991: Documentation for a linear drag, spherical grid, cavitating fluid sea ice model. Ice-Ocean Dyanamics Laboratory Report, 91–2, Thayer School of Engineering, Dartmouth College.

——, and W. D. Hibler III, 1989: The effect of ice pressure on marginal ice zone dynamics. *IEEE Trans. on Geoscience and Remote Sensing,* **27,** 514–521.

——, and ——, 1990: On a simple sea ice dynamics model for climate studies. *Ann. Glaciol.*, **14,** 72–77.

Hibler, W. D., III, 1979: A dynamic thermodynamic sea ice model. *J. Phys. Oceanogr.*, **9,** 817–846.

——, 1980: Modeling a variable thickness sea ice cover. *Mon. Wea. Rev.* **108,** 1943–1973.

——, and J. E. Walsh, 1982: On modeling seasonal and interannual fluctuations of Arctic sea ice. *J. Phys. Oceanogr.*, **12,** 1514–1523.

——, and K. Bryan, 1987: A diagnostic ice-ocean model. *J. Phys. Oceanogr.*, **17,** 987–1015.

Ip, C. F., W. D. Hibler III, and G. M. Flato, 1991: On the effect of rheology on seasonal sea ice simulations. *Ann. Glaciol.*, **15,** 17–25.

Jenkins, G. M., and D. G. Watts, 1968: *Spectral Analysis and Its Applications.* Holden-Day, 525 pp.

Maykut, G. A., and N. Untersteiner, 1971: Some results from a time dependent, thermodynamice model of sea ice. *J. Geophys. Res.*, **76,** 1550–1575.

McPhee, M. G., 1975: Ice–ocean momentum transfer for the AIDJEX ice model. *AIDJEX Bull.*, **29,** 93–111.

McLaren, A. S., 1989: The under-ice thickness distribution of the

Arctic basin as recorded in 1958 and 1970. *J. Geophys. Res.*, **94,** 4971–4983.

Nikiforov, Y. G., Z. M. Gudkovich, Y. I. Yefimov, and M. A. Romanov, 1967: Principles of a method for calculating the ice redistribution under the influence of wind during the navigation period in arctic seas. *Trudy Arkticheskii i Antarkticheskii Nauchnoissledovatel'skii Institut,* Leningrad, 257, 5–25 (Transl.: *AIDJEX Bull.*, **3,** 40–64, 1970).

Parkinson, C. L., and W. M. Washington, 1979: A large-scale numerical model of sea ice. *J. Geophys. Res.*, **84,** 311–337.

Walsh, J. E., W. D. Hibler III, and B. Ross, 1985: Numerical simulation of Northern Hemisphere sea ice variability, 1951–1980. *J. Geophys. Res.*, **90**(C3), 4847–4865.

Semtner, A. J., Jr., 1976: A model for the thermodynamic growth of sea ice in numerical investigations of climate. *J. Phys. Oceanogr.*, **6,** 379–389.

——, 1987: A numerical study of sea ice and ocean circulation in the Arctic. *J. Phys. Oceanogr.*, **17,** 1077–1099.

Stommel, H., 1948: The westward intensification of wind-driven ocean currents. *Trans. Amer. Geophys. Union,* **29,** 202–206.